Published in final edited form as:
Nat Immunol. 2021 February 01; 22(2): 179–192. doi:10.1038/s41590-020-00848-3.

Distinct metabolic programs established in the thymus control effector functions of γδ T cell subsets in tumor microenvironments

Noella Lopes[1,8], **Claire McIntyre**[2,8], **Stefania Martin**[3,8], **Mathilde Raverdeau**[4,8], **Nital Sumaria**[3], **Ayano C. Kohlgruber**[2], **Gina J. Fiala**[1], **Leandro Agudelo**[7], **Lydia Dyck**[4], **Harry Kane**[2,4], **Aaron Douglas**[4], **Stephen Cunningham**[4], **Hannah Prendeville**[4], **Roisin Loftus**[4], **Colleen Carmody**[2], **Philippe Pierre**[5,6], **Manolis Kellis**[7], **Michael Brenner**[2], **Rafael J. Argüello**[5], **Bruno Silva-Santos**[1,9], **Daniel J. Pennington**[3,9], **Lydia Lynch**[2,4,9]

[1]Instituto de Medicina Molecular João Lobo Antunes, Faculdade de Medicina, Universidade de Lisboa, Lisbon, Portugal [2]Brigham and Women's Hospital, Harvard Medical School, Boston MA, USA [3]Blizard Institute, Barts and The London School of Medicine, Queen Mary University of London, London, E1 2AT, UK [4]Trinity Biomedical Science Institute, Trinity College Dublin, Dublin, Ireland [5]Aix Marseille Université, CNRS, INSERM, CIML, Centre d'Immunologie de Marseille-Luminy, Marseille, France [6]Institute for Research in Biomedicine (iBiMED) and Ilidio Pinho Foundation, Department of Medical Sciences, University of Aveiro, 3810-193 Aveiro, Portugal [7]MIT Computer Science and Artificial Intelligence Laboratory, MA, USA

Abstract

Metabolic programming controls immune cell lineages and functions, but little is known about γδ T cell metabolism. Here, we found that γδ T cell subsets making either interferon-γ (IFN-γ) or interleukin-17 (IL-17) have intrinsically distinct metabolic requirements. Whereas IFN-γ^+ γδ T cells were almost exclusively dependent on glycolysis, IL-17^+ γδ T cells strongly engaged oxidative metabolism, with increased mitochondrial mass and activity. These distinct metabolic signatures were surprisingly imprinted early during thymic development, and were stably maintained in the periphery and within tumors. Moreover, pro-tumoral IL-17^+ γδ T cells selectively showed high lipid uptake and intracellular lipid storage, and were expanded in obesity,

Correspondence to: Daniel J. Pennington.

Correspondence should be addressed to D.J.P. (d.pennington@qmul.ac.uk).
[8]These authors contributed equally to this work.
[9]These authors contributed equally to this work.

Author contributions

N.L, C.M, S.M and M.R performed most of the experiments and analyzed the data. G.J.F. designed and performed some experiments. N.S., A.C.K., L.D., H.K., A.D., S.C., H.P. R.L. and C.C. provided technical assistance in some experiments. M.K. and L.A performed bioinformatic analysis and M.B provided reagents, materials and support. P.P. and R.J.A. provided key assistance with the SCENITH™ methodology. B.S.-S., D.J.P and L.L conceived and supervised the study. N.L, C.M., B.S.-S., D.J.P. and L.L. wrote the manuscript.

Competing interests

B.S.-S. is an inventor of the patented "Delta One T cell" technology, which has been acquired by GammaDelta Therapeutics (London, UK).

Europe PMC Funders Author Manuscripts

and in tumors of obese mice. Conversely, glucose supplementation enhanced the anti-tumor functions of IFN-γ$^+$ γδ T cells and reduced tumor growth upon adoptive transfer. These findings have important implications for the differentiation of effector γδ T cells and their manipulation in cancer immunotherapy.

Introduction

T cells engage specific metabolic pathways to support their differentiation, proliferation and function[1,2]. Whereas naive αβ T cells oxidize glucose-derived pyruvate *via* oxidative phosphorylation (OXPHOS) or fatty acid oxidation (FAO) to generate ATP, most effector αβ T cells engage in aerobic glycolysis ("Warburg effect"), i.e. the conversion of glucose to lactate, to strengthen cell growth and proliferation[3]. On the other hand, while aerobic glycolysis is required for optimal αβ T cell effector function[4,5], tumor cells heavily consume glucose in the tumor microenvironment (TME), which has a dramatic impact on cytokine production by T cells and hampers tumor immunity[5,6]. There is therefore great interest in understanding how metabolism-based interventions could inhibit tumor metabolism while promoting effective anti-tumor immunity for improved immunotherapeutic outcomes[7].

γδ T cells represent a promising immune population for next-generation cancer immunotherapies[8,9]. Since they are not MHC-restricted nor dependent on neoantigen recognition, γδ T cells constitute a complementary layer of anti-tumor immunity to their αβ T cell counterparts[10]. In fact, many properties of γδ T cells, including sensing of "stress-inducible" changes and very rapid effector responses, align best with innate immunity, or "lymphoid stress-surveillance"[11], although in some instances they display adaptive-like behaviour and profound shaping of their T cell receptor (TCR) repertoires[12,13].

The effector functions of murine γδ T cells are dominated by the production of two key cytokines, interleukin 17A (IL-17) and interferon-γ (IFN-γ). Beyond contributions to immune responses against pathogens, the provision of these two cytokines by γδ T cells is important in many (patho)physiological contexts, such as maintenance of tissue homeostasis[14,15], autoimmunity[16] and cancer[8]. IL-17 and IFN-γ are mostly produced by distinct γδ T cell subsets that, unlike their CD4$^+$ T cell counterparts, typically acquire their effector functions during thymic development[17,18]. Thymic γδ T cell progenitors, driven by signals including those stemming from the T cell receptor (TCR), split into a CD27$^+$ (and CD45RB$^+$) branch that makes IFN-γ but not IL-17; and a CD27$^-$ (and CD44^{hi}) pathway that selectively expresses IL-17[17–21].

The IFN-γ/IL-17 dichotomy between effector γδ T cell subsets is particularly relevant in cancer, since IFN-γ-producing γδ T cells (γδ^{IFN}) are associated with tumor surveillance and regression, whereas IL-17-secreting γδ T cells (γδ^{17}) promote primary tumor growth and metastasis, both in mice and in humans[8,22]. However, the molecular cues that regulate the balance between such antagonistic γδ T cell subsets in the TME remain poorly characterized. Given the strong impact of metabolic resources on anti-tumor αβ T cell responses, here we have investigated the metabolic profiles of γδ T cell subsets and how they might impact on their activities in the TME. We find here that γδ^{IFN} T cells are almost exclusively glycolytic, whereas γδ^{17} T cells are strongly dependent on mitochondrial and

Europe PMC Funders Author Manuscripts

lipid oxidative metabolism. This metabolic dichotomy is established in the thymus during γδ T cell development, and maintained in peripheral lymphoid organs and within tumors in various experimental models of cancer. We further show that the provision of glucose or lipids has major impact on the relative expansion and function of the two γδ T cell subsets, and this can be used to enhance anti-tumor γδ T cell responses.

Results

Intra-tumoral γδ T cell subsets display distinct metabolic profiles

The analysis of metabolic profiles of tumor-infiltrating γδ lymphocytes (γδ TILs) presented a major challenge: the low numbers that can be retrieved from tumor lesions in mice are largely incompatible with techniques such as Seahorse metabolic flux analysis. To overcome this difficulty, we used a newly developed protocol, SCENITH™ (*Single Cell mEtabolism by profiling Translation inHibition)*, which is a flow cytometry-based method for profiling energy metabolism with single cell resolution[23]. This method is based on metabolism-dependent translation rates and puromycin's incorporation into nascent proteins (Extended Data Fig. 1). The use of specific inhibitors allows the estimation of glucose dependence, mitochondrial dependence, glycolytic capacity and fatty acid and amino acid oxidation (FaaO) capacity. We employed SCENITH™ to analyze the metabolic profiles of γδ TILs isolated from tumor lesions in well-established mouse models of breast (E0771) and colon (MC38) cancer. In both cancer models, and at both later (Fig. 1a,b) and earlier time points (Fig. 1c,d), we observed that $\gamma\delta^{IFN}$ cells had substantially higher glycolytic capacity, whereas $\gamma\delta^{17}$ cells were strongly dependent on mitochondrial activity (Fig. 1). These data, obtained in cancer models, prompted us to investigate the metabolic phenotypes of γδ T cell subsets in multiple tissues at steady state.

Peripheral γδ T cell subsets show different mitochondrial and metabolic phenotypes

To explore the metabolic differences between γδ T cell subsets in peripheral tissues, we analysed mitochondria, given their central role in cellular metabolism. To distinguish between $\gamma\delta^{IFN}$ and $\gamma\delta^{17}$ cells we used CD27 expression[18–21]. $CD27^{-}$ γδ ($\gamma\delta^{17}$) cells displayed increased mitotracker and tetramethylrhodamine methyl ester (TMRM) staining in peripheral lymph nodes (LNs) compared to $CD27^{+}$ γδ ($\gamma\delta^{IFN}$) cells, indicating higher mitochondrial mass (normalized to cell size) and mitochondrial membrane potential ($\Delta\Psi m$), respectively (Fig. 2a,b). These differences were retained upon activation and expansion *in vitro* (Extended Data Fig. 2). Importantly, the distinct mitochondrial phenotypes were also validated with another mitochondrial membrane potential dye, tetramethylrhodamine ethyl ester (TMRE), and were features of $\gamma\delta^{17}$ and $\gamma\delta^{IFN}$ cells *ex vivo* from multiple locations (Fig. 2c). In agreement with mitochondrial enrichment in $\gamma\delta^{17}$ cells, seahorse metabolic flux analysis of peripheral γδ T cells showed higher levels of basal OXPHOS in $\gamma\delta^{17}$ cells, and conversely, increased basal levels of glycolysis in $\gamma\delta^{IFN}$ cells (Fig. 2d-f). These data were validated in independent experiments using SCENITH™ on splenic and LN γδ T cell subsets (Fig. 2g).

To assess if this metabolic dichotomy had an underlying transcriptional basis, we measured the mRNA levels of key mitochondrial and glycolysis-associated genes in purified peripheral

γδ^{17} and γδ^{IFN} cells. We found systematic biases in gene expression that matched the differential metabolic programs (Fig. 2h,i). Of particular note is the clear-cut segregation of two master transcriptional regulators: *Nrf1*, which orchestrates mitochondrial DNA transcription[24,25], found to be enriched in γδ^{17} cells (Fig. 2h); and *Myc*, which controls glycolysis[26,27], that was highly overexpressed in γδ^{IFN} cells (Fig. 2i). Myc expression was further validated using a Myc-GFP reporter mouse (Fig. 2j). These data collectively demonstrated that γδ T cell subsets possess distinct mitochondrial and metabolic features in peripheral organs at steady state.

γδ T cell subsets are metabolically programmed in the thymus

We next aimed to understand when, during their differentiation, the metabolic differences between the two effector γδ T cell subsets were established. Since most γδ T cells are functionally pre-programmed in the thymus, we examined γδ thymocyte sub-populations. Studies have identified sequential stages of thymic γδ T cell progenitor development marked by CD24, CD44 and CD45RB[19]. Early CD24^{+} (γδ^{24+}) precursors downregulate CD24 to become a CD24^{-}CD44^{-}CD45RB^{-} (γδ^{TN}) population that generates cells committed to either IL-17 or IFN-γ expression, which display respectively CD44^{hi}CD45RB^{-} (γδ^{17}) and CD44^{+}CD45RB^{+} (γδ^{IFN}) phenotypes (Extended Data Fig 3). By using SCENITH™, we found that, in both the adult (Fig. 3a) and newborn (Fig. 3b) thymus, these subsets showed the same metabolic dichotomy as in the periphery (Fig. 2g), although this was less distinct in γδ thymocytes, likely due to the dynamic subset segregation process[19].

To investigate any potential switching of metabolic programming during γδ thymocyte development, we first compared early thymic γδ progenitors with more mature subpopulations already committed to IL-17 or IFN-γ production. We found that γδ^{24+} and γδ^{TN} progenitors stained highly for TMRE, that was lost when ΔΨm was dissipated by the ionophore carbonyl cyanide-4-(trifluoromethoxy) phenylhydrazone (FCCP) (Fig. 3c,d). Although γδ^{17} cells retained a high level of TMRE staining, γδ^{IFN} cells showed a marked reduction in ΔΨm suggesting a metabolic switch away from OxPhos (Fig. 3d). Moreover, imagestream analysis of γδ^{17} cells stained with either mitotracker or TMRE revealed large and active mitochondria, in contrast with γδ^{IFN} cells that displayed negligible staining for either dye (Fig. 3e), in line with our previous observations in peripheral subsets (Fig. 2a-c). Furthermore, Seahorse extracellular flux analysis showed that γδ^{17} thymocytes have both higher maximal respiration potential and spare respiratory capacity than their γδ^{IFN} counterparts (Fig. 3f,g). Thus, γδ T cell subsets acquire distinct mitochondrial features during their acquisition of effector function in the thymus.

The adoption of divergent metabolic programs by thymic γδ T cell subsets suggested they could thrive under distinct metabolic environments. To begin to address this, we placed WT E15 thymic lobes in 7-day fetal thymic organ cultures (E15 + 7d FTOC) with media containing either low or high amounts of glucose (Fig. 3h). γδ^{17} cells were readily detected in lower glucose conditions but failed to develop to normal numbers when glucose concentrations were raised. By contrast, γδ^{IFN} cells were relatively enriched in high glucose conditions as demonstrated by a significant decrease in the γδ^{17}/γδ^{IFN} cell ratio (Fig. 3h).

We next established E15 + 7d FTOC in the presence of the glycolysis inhibitor 2-deoxy-D-glucose (2-DG), and found increased numbers of $\gamma\delta^{17}$ cells and increased $\gamma\delta^{17}/\gamma\delta^{IFN}$ cell ratios (Fig. 3i). A similar result was observed in E15 + 7d FTOC when cultured with Fasentin that blocks glucose uptake (Extended Data Fig. 4). By contrast, running E15 + 7d FTOC in the presence of metformin, which reduces the efficiency of OxPhos by inhibiting complex I of the electron transport chain, impaired $\gamma\delta^{17}$ cell generation and decreased the $\gamma\delta^{17}/\gamma\delta^{IFN}$ cell ratio (Fig. 3j). Collectively, these results suggest that the mitochondrial characteristics adopted by $\gamma\delta^{17}$ and $\gamma\delta^{IFN}$ cells during thymic development directly impact their ability to thrive in distinct metabolic environments.

Distinct mitochondrial activities underlie effector fate of thymic γδ T cell precursors

We next aimed to investigate the association of distinct metabolic programs with the developmental divergence of $\gamma\delta^{17}$ and $\gamma\delta^{IFN}$ cells in the thymus. Although the $\gamma\delta^{TN}$ population, i.e. the progenitor γδ cell subset that immediately precedes the surface upregulation of either CD44 or CD45RB (marking commitment to the IL-17 or IFN-γ pathways, respectively[19]) was predominantly $TMRE^{hi}$, we observed a fraction of cells with reduced TMRE staining that we reasoned might be transitioning to the $TMRE^{lo}$ state shown by $\gamma\delta^{IFN}$ cells (Fig. 3c). We further hypothesized that the metabolic status of $\gamma\delta^{TN}$ progenitors may predict their developmental fate. To test this, we sorted $TMRE^{hi}$ and $TMRE^{lo}$ cells from the $\gamma\delta^{TN}$ subset obtained from E15 + 7d FTOC, and cultured them for 5-days on OP9-DL1 cells that are known to support appropriate development of thymocytes[28]. As predicted, virtually all cells from the $TMRE^{lo}$ cultures upregulated CD45RB and entered the IFNγ-pathway (Fig. 4a); however, we were surprised that almost all cells from the $TMRE^{hi}$ cultures entered the $CD44^{hi}$ IL-17-pathway (Fig. 4a). This strongly suggests that $\gamma\delta^{TN}$ cells have already committed to an effector fate, and that this commitment associates with distinct mitochondrial activities.

To pursue this hypothesis further, we tested $\gamma\delta^{24+}$ progenitors that immediately precede the $\gamma\delta^{TN}$ subset; again, we observed a segregation of effector fate, with the majority of $TMRE^{lo}$ $\gamma\delta^{24+}$ cells entering the IFNγ-pathway, and the majority of $TMRE^{hi}$ $\gamma\delta^{24+}$ cells entering the IL-17-pathway (Fig. 4b). The observation that so few $TMRE^{hi}$ $\gamma\delta^{24+}$ cells adopt an IFNγ-secreting fate again suggests that most $\gamma\delta^{24+}$ progenitors have already committed to subsequent effector function. Moreover, we found that differences in TMRE levels correlated with the known[18,20,21] effector biases of $V\gamma1^+$ ($\gamma\delta^{IFN}$-biased) and $V\gamma4^+$ ($\gamma\delta^{17}$-biased) progenitors (Fig. 4c); and allowed TMRE-based segregation of effector fates using only $V\gamma4^+$ progenitors (Extended Data Fig. 5). Furthermore, among $\gamma\delta^{24-}$ thymocytes along the $\gamma\delta^{IFN}$ pathway, we observed a progressive downregulation of TMRE levels from $\gamma\delta^{TN}$ to $CD44^{-}CD45RB^{+}$ cells and finally $\gamma\delta^{IFN}$ cells (Fig. 4d).

Given that we and others[20,21] have previously shown a key role for TCR signalling in $\gamma\delta^{IFN}$ thymocyte differentiation, we next asked if downregulation of TMRE levels associated with hallmarks of TCR signalling. Indeed, we found that low TMRE associated with high expression of CD73 (Fig. 4e), one of the best established markers of TCR signalling in γδ T cell development[20,28,29]. Moreover, in E15 thymic lobes, TMRE staining was reduced along with CD25 downregulation, which is another hallmark of (developmentally early) TCRγδ

signalling[18,20,21] (Fig. 4f). Furthermore, at this E15 stage, the cells with the lowest TMRE staining were V$\gamma5^+$ progenitors (Fig. 4f) that are known to engage a Skint1-associated TCR-ligand in the thymus and to uniformly commit to the IFNγ-pathway[30].

These lines of evidence suggested that $\gamma\delta$ progenitors receiving agonist TCR$\gamma\delta$ signals shift away from OxPhos as indicated by their reduced $\Delta\Psi m$. To strengthen this point, we manipulated TCR signals using agonist GL3 mAb, which, as expected[18,19], promoted $\gamma\delta^{IFN}$ cell development while inhibiting the $\gamma\delta^{17}$ pathway in E17 + 6d FTOC (Fig. 4g). Upon specifically sorting TMRE^{hi} $\gamma\delta^{24+}$ cells from E17 thymi and stimulating them with GL3 for 5h, we found a subpopulation that downregulated CD24 together with TMRE levels, in a mAb dose-dependent manner (Fig. 4h). These results strongly suggest that TCR signalling leads to $\Delta\Psi m$ downregulation as $\gamma\delta$ thymocytes differentiate into IFN-γ producers.

To gain further molecular resolution, we performed single-cell RNAsequencing on TMRE^{lo} and TMRE^{hi} $\gamma\delta^{24+}$ cells from E15 + 2d FTOC (Extended Data Fig. 6a). Dimensionality reduction using UMAP showed that TMRE^{lo} cells clustered clearly away from TMRE^{hi} $\gamma\delta^{24+}$ cells (Fig. 4i), and the former were enriched in genes involved in the regulation of antigen receptor signalling (Fig. 4j). In support of the metabolic phenotypes observed *ex vivo*, genes associated with OxPhos were enriched specifically in TMRE^{hi} $\gamma\delta^{24+}$ cells while genes involved in glucose metabolism were unregulated in TMRE^{lo} $\gamma\delta^{24+}$ cells (Extended Data Fig. 6b).

These data collectively demonstrate that metabolic status of thymic $\gamma\delta$ progenitors marks their developmental fate from a very early stage. Progenitors entering the IL-17 pathway display sustained high mitochondrial activity, whereas those in the IFN-γ pathway undergo a TCR-induced metabolic shift towards aerobic glycolysis. We next questioned how these intrinsic metabolic differences impacted the physiology of effector $\gamma\delta$ T cell subsets.

Enrichment of lipid storage and lipid metabolism in $\gamma\delta^{17}$ cells

Having shown that, in stark contrast to $\gamma\delta^{IFN}$ cells, $\gamma\delta^{17}$ cell generation was reduced under high glucose concentrations (Fig. 3h), and enhanced upon inhibition of glycolysis (Fig. 3i) or glucose uptake (Extended Data Fig. 4), we questioned whether other metabolic resources may be important for $\gamma\delta^{17}$ cell physiology. To address this question we took advantage of *Zbtb16*^{GFP} reporter mice to segregate $\gamma\delta^{17}$ and $\gamma\delta^{IFN}$ cells (*Zbtb16* encodes the transcription factor PLZF[21,14,31]). We performed RNA-sequencing of lymphoid and tissue-resident $\gamma\delta$ T cells sorted into PLZF$^+$ ($\gamma\delta^{17}$) and PLZF$^-$ ($\gamma\delta^{IFN}$) cells (Extended Data Fig. 7a). As expected, $\gamma\delta^{17}$ cells across tissues expressed *Il17a*, whereas *Il17f* was also expressed in tissue-resident $\gamma\delta^{17}$ cells (Fig. 5a). Different metabolic pathways were associated with lymphoid *versus* tissue resident $\gamma\delta$ T cells. However, the genes common to $\gamma\delta^{17}$ cells across all tissues were related to lipid and mitochondrial metabolism, including glutamate transporter (*Slc1a1*), glucose/fatty acid metabolism (*Pdk4*), mitochondrial protein transport (*Ablim3*) and lipid metabolism (*Fabp1*, *Abdh5*, *Atp10a*). These data highlight genes associated with lipid metabolism as a common feature of $\gamma\delta^{17}$ T cells across tissues. Consistent with this, LN $\gamma\delta^{17}$ cells had a higher neutral lipid content (assessed by LipidTOX staining) than $\gamma\delta^{IFN}$ cells (Fig. 5b). This differential lipid content was further increased upon activation with IL-1β+IL-23 (Extended Data Fig. 7b), was associated with expression

of IL-17A, IL-17F and RORγt (Extended Data Fig. 7c), and was observed across γδ T cells from multiple tissues, with the notable exception of the skin (Fig. 5c), where γδ T cells have been shown to display specific mechanisms of tissue adaptation[32]. In particular, Vγ6$^+$ γδ T cells in the dermis are transcriptionally distinct from those in pLNs and display a highly activated but less proliferative phenotype. This tissue adaptation may alter the metabolic requirements of skin-resident γδ T cells and γδ T cells may adapt to utilize specific metabolites present within the skin[33].

Imaging analysis revealed that the increased LipidTOX staining was due to the accumulation of intracellular lipid droplets in γδ^{17} cells (Fig. 5d,e). Lipid droplets store neutral lipids including triglycerides (TAGs) and cholesterol esters[34]. The two γδ T cell subsets had equivalent TAG content (Fig. 5f) but free cholesterol, as determined by Filipin III staining, was higher in γδ^{17} cells (Fig. 5g). We next questioned if γδ^{17} cells engaged in lipid uptake which could account for lipid storage. Using labelled palmitate (Bodipy-FL-C_{16}), we found that γδ^{17} cells selectively took up lipids (Fig. 5h), which was further enhanced following activation (Extended Data Fig. 7d). Analysis of γδ T cell cytokine production confirmed that the ability to take up palmitate was specific to IL-17 producers (Fig. 5i,j). Of note, Vγ4$^+$ and Vγ6$^+$ (Vγ1$^-$Vγ4$^-$) γδ T cells showed a higher palmitate uptake than Vγ1$^+$ cells (Fig. 5k). While Vγ6$^+$ γδ T cells primarily produce IL-17, Vγ4$^+$, can produce either IFN-γ or IL-17[18,19]. However, palmitate uptake was specific to Vγ4$^+$ cells that produced IL-17 (Fig. 5l). Furthermore, γδ^{17} cells also displayed higher uptake of fluorescently labelled cholesterol ester (Bodipy CholEsteryl FL-C_{12}) (Fig. 5m), emphasizing their ability to take up multiple types of lipids including fatty acids and cholesterol.

These data demonstrate that γδ^{17} cells have an exquisite capacity to take up and accumulate intracellular lipids, and display transcriptional signatures of enhanced lipid metabolism compared to γδ^{IFN} cells.

High fat diet promotes γδ^{17} cell expansion and their accumulation in tumors

We next tested the effect of a lipid-rich, high fat diet (HFD), on γδ T cell subsets *in vivo*. Unlike standard fat diet (SFD) fed mice, which alternate between using lipids or carbohydrates for fuel during light/dark cycles respectively, feeding mice a HFD reduced their respiratory exchange ratio (RER), illustrating a systemic metabolic switch to constantly burning lipids as the main fuel source. (Fig. 6a). We found that both the percentage and absolute number of LN γδ T cells were increased during HFD (Fig. 6b), which was due to a specific increase in γδ^{17} (but not γδ^{IFN}) cells (Fig. 6c,d).

Tumors are another site reported to be lipid-rich. To explore the effect of the lipid-rich tumor environment on γδ^{17} cells, we employed the B16F10 melanoma model. In SFD mice, we found an enrichment of γδ^{17} cells within the tumor compared to draining LN (dLN) or spleen (Fig. 6e). These γδ^{17} cells were also enriched compared to γδ^{IFN} cells (Fig. 6f). Given γδ^{17} were enriched in obese mice and in the tumor, we next asked if obesity combined with the tumor model would further increase γδ^{17} cells. Mice fed HFD exhibited enhanced tumor growth (Fig. 6g), and further increased percentages and numbers of tumor-infiltrating γδ^{17} cells compared to the SFD group (Fig. 6 h-j). These data demonstrate that a lipid-rich environment selectively accumulates γδ^{17} cells but not γδ^{IFN} cells in the tumor.

Given the preferential uptake of cholesterol by γδ^{17} cells (Fig. 5i), we next investigated its effect on γδ^{17} cell proliferation and function. We incubated purified γδ^{27-} (γδ^{17}) cells with cholesterol-loaded cyclodextrin (CLC), which we found to promote γδ^{27-} cell proliferation when compared to control culture conditions (Fig. 6k). To determine its impact on tumor growth *in vivo*, we injected CLC pre-treated (or control) γδ^{17} cells twice (within two days) into s.c. E0771 tumors (as established in Fig. 1b), which allow local T cell delivery. Strikingly, γδ^{17} cells pre-treated with CLC substantially enhanced tumor growth (Fig. 6l-n).

Conversely, we also tested the effect of reducing lipids *in vivo*, by injected orlistat, which inhibits lipases and thus prevents uptake of dietary fat, into B16F10 tumor-bearing mice. Mice injected with orlistat exhibited reduced body weight and tumor growth compared to vehicle-treated mice (Extended Data Fig. 7a,b). Importantly, these mice showed decreased numbers of tumor-infiltrating γδ^{17} cells, which had lower neutral lipid content (Extended Data Fig. 7c,d). Together, these data show that lipid-rich environments promote the selective expansion of γδ^{17} cells that support tumor growth.

Glucose supplementation enhances anti-tumor functions of γδ^{IFN} cells

We next aimed to use the knowledge gathered in this study to boost anti-tumor γδ T cell responses, which are known to rely on γδ^{IFN} cells[8,22]. Given our data showing that glucose promotes the development of γδ^{IFN} over γδ^{17} cells in the thymus (Fig. 3h,i), and the higher glycolytic capacity of γδ^{IFN} cells in peripheral organs (Fig. 2g) and also within tumors (Fig. 1b-e), we hypothesized that glucose supplementation would enhance γδ^{IFN} cell functions. Further supporting this hypothesis, we found that intra-tumoral γδ^{IFN} cells preferentially took up fluorescently labeled glucose (2-NDBG) when compared to γδ^{17} TILs (Fig. 7a).

We first tested the impact of glucose on γδ^{17} and γδ^{IFN} cell functions *in vitro*. We cultured purified γδ^{27-} (γδ^{17}) or γδ^{27+} (γδ^{IFN}) cells in standard culture conditions containing low dose glucose (5mM) or in high glucose (50mM). We found high glucose to be detrimental to γδ^{17} cells (Extended Data Fig. 8), in stark contrast to γδ^{IFN} cells. Indeed, supplementation with high glucose augmented (whereas provision of 2-DG reduced) the percentage and numbers of γδ^{IFN} cells (Fig. 7b), with parallel effects on their proliferation (Fig. 7c) and on the levels of expression of both IFN-γ (Fig. 7d) and its master transcriptional regulator[21], T-bet (Fig. 7e).

To specifically address the importance of aerobic glycolysis for γδ^{IFN} cells, we cultured γδ^{IFN} cells with galactose (compared to glucose), since cells grown in galactose enter the pentose phosphate pathway instead of using aerobic glycolysis[35,36]. We observed a reduction in the percentage and absolute numbers of γδ^{IFN} cells (Fig. 7f), as well as in their IFN-γ (Fig. 7g) and T-bet (Fig. 7h) expression levels, thus establishing that aerobic glycolysis is required for optimal IFN-γ production by γδ^{IFN} cells.

Next we asked if the cytotoxic function of γδ^{IFN} cells was also enhanced by glucose supplementation. For this, we co-cultured γδ^{IFN} cells that were previously supplemented (or not) with high dose of glucose with E0771 breast cancer cells at different effector:target (E:T) ratios. “Glucose-enhanced” γδ^{IFN} cells displayed substantially higher cytotoxic

potency against the cancer cells, compared to the respective controls at each E:T ratio (Fig. 7i).

As γδ T cells are actively being pursued in the clinic as an adoptive cell therapy for cancer[8], we tested whether we could use glucose supplementation to enhance the anti-tumor functions of $\gamma\delta^{IFN}$ cells *in vivo*, in an adoptive cell transfer setting. Purified $\gamma\delta^{IFN}$ cells were cultured in the presence or absence of high dose glucose for 5h, washed, and injected twice (within two days) into the tumor site. While control $\gamma\delta^{IFN}$ cells produced a small yet significant reduction in tumor size, glucose substantially augmented the anti-tumor effects of $\gamma\delta^{IFN}$ cells, essentially inhibiting tumor growth (from the time of injection) within the time window analysed (Fig. 7j,k). These data reveal a new, metabolism-based, means to enhance the anti-tumor functions of γδ T cells that could be explored for adoptive cell immunotherapy of cancer.

Discussion

Metabolism dysregulation is viewed as an immune evasion strategy in cancer. To overcome it, and thus enable anti-tumor immune responses, it is critical to understand immune cell metabolism and its interplay with tumor cells in the TME. Although our knowledge on αβ T cell metabolism has increased significantly[1,3,37], little is known about γδ T cells. Here, we identified a metabolic dichotomy between the main effector γδ T cell subsets that play opposing roles in cancer immunity[8,22]. Whereas anti-tumoral $\gamma\delta^{IFN}$ cells are almost exclusively glycolytic, pro-tumoral $\gamma\delta^{17}$ cells require mitochondrial metabolism; and their activities within tumors can be promoted by glucose or lipid metabolism, respectively.

Unexpectedly, the metabolic dichotomy of γδ T cell subsets is established early during thymic development, which contrasts with the peripheral metabolic (re)programming of effector αβ T cells. Naïve αβ T cells require activation to undergo rewiring of cellular metabolism, namely transition from OxPhos to aerobic glycolysis, through which glucose is fermented into lactate rather than oxidized in mitochondria[3]. Furthermore, depending on metabolic cues in the tissue or during immune challenge, naïve T cells are pushed toward Th1, Th2, Th17 or Treg fates, dependent on intrinsic metabolic pathways engaged outside the thymus. By contrast, we show that an equivalent metabolic shift occurs in early thymic γδ progenitors as they commit to the IFN-γ pathway, seemingly as a result of strong TCRγδ signalling. Indeed, analysis of various hallmarks of TCR signalling suggest that γδ progenitors receiving agonist TCRγδ signals shifted away from OxPhos as indicated by their reduced $\Delta\Psi m$. Moreover, upon TCR (GL3 mAb) stimulation, a small population of γδ progenitors downregulated CD24 together with $\Delta\Psi m$ (TMRE), thus associating strong TCRγδ signalling in the $\gamma\delta^{IFN}$ developmental pathway with metabolic reprogramming. This draws a parallel with αβ T cell activation, during which early TCR signalling is required for induction of aerobic glycolysis[38]. This acts as a switch for *Myc* mRNA (and protein) expression, such that strength of TCR stimulus determines the frequency of T cells that transcribe *Myc* mRNA[36]. The common denominator of the metabolic switches in effector γδ and αβ T cells may thus be upregulation of Myc, which is required for transcription of genes encoding glycolytic enzymes[26,27]. Indeed, our data show a striking enrichment of Myc (mRNA and protein) in $\gamma\delta^{IFN}$ cells compared to $\gamma\delta^{17}$ cells. On the other hand, the

sustained dependence of γδ^{17} cells on mitochondrial OxPhos is in line with that recently reported for their functional αβ T cell equivalents, Th17 cells[39]. Of note, IL-17-producing type 3 innate lymphoid cells (ILC3) were recently shown to require both glycolysis and mitochondrial-derived ROS for activation[40], but a direct comparison with type 1 ILCs is still missing.

The concept of TCR signalling playing a key role in the metabolic programming of γδ T cell subsets builds upon, but provides a novel perspective to, previous models of their thymic development. Thus, the unequivocal dependence on strong TCR signals for γδ^{IFN} cell differentiation[20,30] may be linked to a required metabolic shift to aerobic glycolysis. Moreover, the detrimental impact of agonist TCR signals on γδ^{17} cell development may be due to metabolic conflict with their OxPhos requirements, documented by our FTOC experiments using specific inhibitors. Importantly, these distinct metabolic phenotypes are maintained in peripheral γδ T cell subsets, which is consistent with and expands our previous epigenetic and transcriptional analyses[41,42].

We were particularly interested to investigate the metabolic properties of peripheral γδ T cell subsets once they infiltrated tumor lesions, for which we employed three experimental models of cancer (melanoma, breast and colon). Critically, we found that the dichotomy between γδ^{17} and γδ^{IFN} subsets was preserved in the TME, which enabled metabolic interventions that may have therapeutic potential. In fact, while γδ T cell infiltration is largely perceived to associate with favourable prognosis in cancer patients[43], recent clinical data have suggested that, in agreement with mouse experimental systems[22], human γδ^{17} *versus* γδ^{IFN} cell subsets have antagonistic prognostic values[8]. Thus, improvement in the therapeutic performance of γδ T cells in the clinic[44] is likely to require a better understanding of the factors that control the balance between γδ^{17} and γδ^{IFN} cell subsets in the TME.

Here, we also identified lipids as key γδ^{17}-promoting factors, which is particularly relevant because tumors are known to be lipid-rich microenvironments[4,5]. Palmitate and cholesterol ester uptake were higher in γδ^{17} than γδ^{IFN} cells. Thus, we propose that the increase in intracellular lipids is due to enhanced uptake, although endogenous lipid synthesis cannot be ruled out. Our findings that γδ^{17} cell proliferation is boosted by cholesterol treatment, and that these cells expand substantially in obese mice, provide additional evidence that HFD causes a systemic increase in the γδ^{17} subset, consistent with previous findings in the skin[45] and lungs[46], and may provide a mechanistic understanding for this expansion. Obesity is a known risk factor for cancer and we previously demonstrated the link between obesity and suppression of NK cell anti-tumor function[47]. Given that γδ^{17} cells have strong pro-tumoral effects and we find this population to be expanded in tumors of obese mice, this may represent an additional mechanism linking cancer and obesity, whereby abundant lipids favor γδ^{17} over γδ^{IFN} cells to support tumor growth.

Conversely, we found γδ^{IFN} cells, from their thymic development to intra-tumoral functions, to be boosted by glucose metabolism. Naturally, the large consumption of glucose by tumor cells[7] creates a major metabolic constraint on γδ^{IFN} TILs. Glucose restriction can impair T cell cytokine production[5,6], while production of lactate by tumor cells performing aerobic

glycolysis can inhibit T cell proliferation and cytotoxic functions[48]. Therefore, we do not conceive glucose supplementation as an appropriate strategy to enhance endogenous T cell (including $\gamma\delta^{IFN}$) responses *in vivo*. Instead, we suggest that it should be considered in protocols used to expand/differentiate γδ T cells *ex vivo* for adoptive cell therapy. Such an "*in vitro* glucose boost" may enable stronger anti-tumor activities (namely, IFN-γ production and cytotoxicity) upon T-cell transfer, as suggested by our data using $CD27^+$ $\gamma\delta^{IFN}$ cells in the breast cancer model, although evaluation of the duration and long-term impact of this "boost" requires further investigation in slower-growing tumor models.

While we did not dissect the mechanistic link between aerobic glycolysis and IFN-γ production by $CD27^+$ $\gamma\delta^{IFN}$ cells, previous studies on αβ T cells have shown that glycolysis controls (via the enzyme GAPDH) the translation of IFN-γ mRNA[5]. Moreover, glycolysis was shown to be essential for the cytotoxic activity of NK cells, namely their degranulation and Fas ligand expression, upon engagement of NK cell receptors (NKRs)[49]. This is particularly interesting when considering the potential of a human γδ T cell product that we developed for adoptive cell therapy of cancer, Delta One T (DOT) cells. These $V\delta1^+$ T cells are induced *in vitro* to express high levels of NKRs that enhance their cytotoxicity and IFN-γ production[9,50]. We therefore propose high dose glucose to be added to the DOT protocol as to further increase their anti-tumor potential.

In sum, this study demonstrates that thymic differentiation of effector γδ T cell subsets, besides well-established epigenetic and transcriptional regulation, includes divergent metabolic programming that is sustained in the periphery and, in particular, in the TME. It further identifies distinct metabolic resources that control the intra-tumoral activities of γδ T cell subsets, with lipids favoring $\gamma\delta^{17}$ cells and glucose boosting $\gamma\delta^{IFN}$ cells, which provides a new metabolism-based angle for therapeutic intervention in cancer and possibly other diseases.

Methods

Ethics statement

All mouse experiments performed in this study were evaluated and approved by the institutional ethical committee (Instituto de Medicina Molecular Orbea), the national competent authority (DGAV) under the license number 019069, UK Home Office regulations and institutional guidelines under license number 70/8758 and by the Institutional Animal Care and Use Committee of Brigham and Women's Hospital and Harvard Medical School, the Trinity College Dublin ethics committee. Euthanasia was performed by CO_2 inhalation. Anesthesia was performed by isoflurane inhalation.

Mice and tumor cell lines

C57Bl/6J (B6) WT mice and Myc-GFP mice (B6;129-$Myc^{tm1Slek}$/J) were purchased from Charles River and Jackson Laboratories. PLZF-GFP (*Zbtb16* ^{GFP}) mice were generated in the laboratory of D. Sant'Angelo as described previously[51]. Mice were maintained under specific pathogen-free conditions. Standard food and water were given *ad libitum*. Where indicated, mice were fed high fat diet (HFD) (Research Diets; D12492) for 8 weeks. Mice

were used at the foetal (embryonic day 14-18), neonatal (1-5 days old) or adult (6-12 weeks old) stages.

The E0771 murine breast adenocarcinoma cells, MC38 murine colon adenocarcinoma cells and B16.F10 melanoma cells were purchased from ATCC (Manassas, VA). Cells were maintained in Dulbecco's Modified Eagle Medium (DMEM) with 10% (vol/vol) FCS (Gibco; Thermo Fisher Scientific) and 1% (vol/vol) penicillin/streptomycin (Sigma-Aldrich).

Tumor transplantation *in vivo*

Mice were injected with 1 x 10^6 E0771 tumor cells in fat pads, 1 x 10^6 MC38 tumor cells or 2 x 10^5 cells B16 tumor cells subcutaneously into the right shaved flank. Tumor growth was measured every 2-3 days using calipers and animals were sacrificed when tumors reached a diameter (D) of 15mm, became ulcerous, or 1 or 2 weeks after tumor injection. Tumor size was calculated using the following formula: $(D1)^2 \times (D2/2)$, D1 being the smaller value of the tumor diameter. In some experiments, mice were fed with a HFD (60% calories from lard) for 10 weeks prior to tumor injection and the HFD was continued throughout the experiment.

Comprehensive Lab Animal Monitoring System

Indirect calorimetry data were recorded using a Promethion Metabolic Cage System (Sable Systems) essentially as described previously[52]. Mice were housed individually in metabolic chambers under a 12h light/dark cycle at room temperature (22°C) with free access to food and water. Mice were acclimated for 24h in metabolic cages before recording calorimetric variables. Mice were fed either a standard chow diet or a high fat (60%) diet *ad libitum* for 8 weeks prior to being placed in metabolic cages and were maintained on either diet throughout the recording.

Tissue processing and cell isolation

Tumors were collected and digested with 1mg/mL collagenase Type I, 0.4 mg/mL collagenase Type IV (Worthington) and 10μg/mL DNase I (Sigma-Aldrich) for 30 minutes at 37°C. Cell suspensions were then filtered through a 100μm nylon cell strainer (Falcon/Corning). γδ T cells were isolated by scratching thymus, spleen and lymph node on a 70μm mesh. Lungs were minced then homogenized in RPMI 1640 using a TissueLyser (Qiagen) and filtered through 70μm mesh. Adipose tissue was processed as described previously[53]. Red blood cells were lysed using RBC Lysis Buffer (Biolegend) or ammonium chloride lysis buffer (made in-house). Single-cell suspensions of fetal and neonatal thymocytes were obtained by gently homogenizing thymic lobes followed by straining through 40μm strainers (BD).

For cell-sorting, γδ T cells were pre-enriched by depletion of $CD4^+$ and $CD8^+$ T cells, dendritic cells and B cells using biotinylated anti-CD4 (RM4-5), anti-CD8 (53-6.7), anti-CD11c (N14) and anti-CD19 (6D5) antibodies with anti-biotin microbeads (Miltenyi Biotech) by QuadroMACS or γδ T cells were purified using TCRγ/δ T Cell Isolation Kit, mouse (Miltenyi Biotec). Cells were sorted on a FACS Aria III (BD Biosciences).

Cell Culture

CD27^{-} γδ T cells were expanded *in vitro* as previously described[54]. This protocol was adapted to expand CD27^{+} γδ T cells by using 10ng/ml IL-2, 10ng/ml IL-15 and 20ng/ml IL-7. For downstream assays, γδ T cells were purified using TCRγ/δ T Cell Isolation Kit, mouse (Miltenyi Biotec). E*x vivo* cultures were performed using RPMI 1640 (Gibco) supplemented with 10% heat-inactivated fetal bovine serum (Gibco), 1% penicillin/streptomycin, 1% L-glutamine. For cytokine stimulation, cells were cultured with 10ng/ml IL-1β and IL-23 (Miltenyi Biotec) and/or IL-12 and IL-18 (BioLegend).

For short-term skin-draining-lymphocyte cultures, single-cell suspensions of lymphocytes were isolated from skin-draining lymph nodes from adult B6 mice. Cells were resuspended in complete RPMI medium (RPMI-1640 with 10% FCS, 1% penicillin and streptomycin, and 2 mM L-glutamine). 1 x 10^{6} lymphocytes in 500μl of complete medium were incubated for 48h in 48-well plates either under control conditions or with the addition of 5-aminoimidazole-4-carboxamide (AICAR; 1.6mM; Sigma-Aldrich). Cells were subsequently analyzed by flow cytometry.

Fetal Thymic Organ Cultures (FTOC)

E15-E17 thymic lobes from B6 mice were cultured on nucleopore membrane filter discs (Whatman) in FTOC medium (RPMI-1640 with 10% FCS, 1% penicillin and streptomycin, 50μM β-mercaptoethanol (Invitrogen), and 2mM L-glutamine (Sigma-Aldrich)) for 6-12 days (unless otherwise indicated). In some experiments 2-deoxyglucose (2-DG; 0.6 mM), fasentin (0.6 mM), metformin (2mM) or oligomycin (1nM) were added to the cultures. All thymic organ cultures were subsequently analysed by flow cytometry. In some cultures, where concentration of glucose was manipulated, “basic” FTOC medium (RPMI-1640 [-] glucose with 10% FCS, 1% penicillin and streptomycin, 50 μM β-mercaptoethanol (Invitrogen), and 2 mM L-glutamine (Sigma-Aldrich)) was used, and glucose was added at 5mM for “low-glucose” conditions or 25mM for “high-glucose” conditions.

In some experiments, anti-TCRδ antibody (GL3; 1μg/ml unless otherwise indicated) was added to the cultures. Cultures containing antibody were rested overnight in fresh FTOC medium before analysis. All thymic organ cultures were subsequently analyzed by flow cytometry.

Manipulation of γδ metabolic pathways *in vitro* and *in vivo*

Spleen and lymph nodes were harvested from C57Bl/6J mice. Cell suspensions were stained with LIVE/DEAD Fixable Near-IR (Thermo Fisher Scientific), anti-CD3ε (145-2C11), anti-TCRδ (GL3), and anti-CD27 (LG.7F9) for 15 minutes at 4°C. CD27^{+} and CD27^{-} γδ T cells were FACS-sorted. CD27^{+} and CD27^{-} γδ T cells were incubated on plate-bound anti-CD3ε (145.2C11) (10μg/mL) in the presence of IL-7 (50μg/mL) or IL-7 (50μg/mL), IL-1β (10μg/mL) and IL-23 (10μg/mL), respectively. All cytokines were purchased from Peprotech. Then, cells were cultured with 2-Deoxy-D-Glucose (2-DG; 2mM; Sigma-Aldrich), high D-glucose (50mM; Sigma-Aldrich), galactose (20mM; Sigma-Aldrich), Carbonyl cyanide 4-(trifluoromethoxy) phenylhydrazone (FCCP; 1μM; Sigma-Aldrich) and cholesterol-loaded cyclodextrin (CLC; 5 μg/mL) for 5h at 37°C for *in vitro* experiments.

For experiments *in vivo*, purified CD27^{-} and CD27^{+} γδ T cells were incubated (or not) for 5h with cholesterol-loaded cyclodextrin (5μg/mL) or with high D-glucose (50mM; Sigma-Aldrich), respectively. 5 x 10^5 CD27^{-} or 1 x 10^6 CD27^{+} γδ T cells were injected twice directly at the tumor site (1st injection 7 days after tumor inoculation and 2nd injection 2 days later). Mice were analyzed 11-days after tumor cell injection.

For lipid depletion *in vivo*, mice were injected daily with 50mg/kg Orlistat i.p. on days 6-9 after tumor injection, then tumor cell infiltrate was analyzed on day-10.

In vitro killing assays

Purified CD27^{+} γδ T cells were supplemented (or not) with high levels of glucose (50mM; Sigma-Aldrich) for 5h at 37°C, 5% CO_2. Then, variable numbers of CD27^{+} γδ T cells were co-cultured with 5 x 10^5 E0771 breast cancer cells in complete RPMI Medium (minus D-Glucose). The killing capacities of CD27^{+} γδ T cells based on death of E0771 cells (Annexin V staining) was assessed by flow cytometry after 24h.

Flow cytometry

γδ T cells were analyzed by flow cytometry using standard procedures. For surface staining, cells were Fc-blocked with anti-CD16/32 (clone 93; eBioscience) and incubated for 15 minutes at 4°C with antibodies and LIVE/DEAD Fixable Near-IR (Thermo Fisher Scientific) or viability dye Zombie NIR stain (BioLegend) in FACs buffer (PBS 1X, 2% FCS, 1mM EDTA). Anti-CD3ε (145-2C11; 1:400), anti-CD27 (LG.7F9; 1:200), anti-CD25 (PC61; 1:400), anti-CD73 (TY/11.8; 1:200) and anti-Vγ2 (UC3-10A6; 1:200) were purchased from eBioscience. Anti-CD45 (30-F11; 1:400), anti-TCRδ (GL3; 1:200), anti-CD24 (M1/69; 1:400), anti-Vγ1 (2.11; 1:100), anti-Vγ4 (UC3-10A6; 1:200), anti-Vγ5 (536; 1:200) and anti-CD45RB (C363-16A; 1:400) were purchased from BioLegend and anti-CD44 (IM7; 1:400) from BD Pharmingen. Cells were washed with FACS buffer. For intracellular cytokine staining, cells were stimulated with 50μg/mL phorbol 12-myristate 13-acetate (PMA; Sigma-Aldrich) and 1μg/mL ionomycin (Sigma-Aldrich) for 3-4 hours at 37°C, 5% CO_2 in the presence of 10μg/mL brefeldin-A (Sigma-Aldrich) and 2μM monensin (eBioscience). Cells were fixed and permeabilized with Foxp3 staining kit (eBioscience/ Thermo Fisher Scientific), according to the manufacturer's instructions. Cells were incubated for 30min at 4°C, with the following antibodies from eBioscience: anti-IFN-γ (XMG1.2; 1:100), Ki67 (SolA15; 1:800), T-bet (4B10; 1:150) and RORγt (B2D; 1:100). Anti- IL-17F (9D3.1C8; 1:100 and IL-17A (TC11-18H10.1; 1:100) were purchased from Biolegend. For Annexin V staining, the Annexin V Kit (eBioscience) was used following the manufacturer's instructions.

The following dyes were purchased from Invitrogen and stained according to manufacturer's instructions: Mitotracker™ Green FM, Tetramethylrhodamine Methyl Ester Perchlorate (TMRM), HCS LipidTOX™ Red Neutral Lipid Stain. Palmitate uptake was measured using 1μM Bodipy FL-C_{16} (Invitrogen) incubated for 10min at 37°C. Cholesterol ester uptake was measured using 2μM Bodipy CholEsteryl FL-C_{12} incubated for 1h at 37°C. Cholesterol content was measured using 50μg/ml Filipin III (Sigma-Aldrich) incubated for 1h at room temperature.

Flow cytometry analysis was performed with a FACS Fortessa, LSRII or Canto II using FACS Diva Software (BD Biosciences) and data analyzed using FlowJo software (BD Biosciences).

Seahorse Metabolic Flux Analysis

Real-time analysis of oxygen consumption rates (OCR) and extracellular-acidification rates (ECAR) of IFN-γ- and IL-17-committed γδ T cells sorted from 5-day-old B6 pups and $CD27^{+/-}$ γδ T cells from spleen/lymph nodes expanded *in vitro* were assessed using the XFp Extracellular Flux or Seahorse XFe-96 analyzers, respectively (Seahorse Bioscience). Cells were added to a Seahorse XF96 Cell Culture Microplate (Agilent), coated with Cell-Tak (Corning) to ensure adherence, and sequential measurements of ECAR and OCR were performed in XF RPMI Seahorse medium supplemented with glucose (10mM), glutamine (2mM), and sodium pyruvate (1mM) following the addition of Oligomycin A (2μM), FCCP (2μM), rotenone (1μM) plus antimycin A (1-4μM). Basal glycolysis, glycolytic capacity, basal mitochondrial respiration and maximal mitochondrial respiration were calculated. OCR and ECAR values were normalized to cell number.

SCENITH™

Cells were plated at 20×10^6 cells/ml in 96-well plates. After activation of γδ T cells, cells were treated for 30 minutes at 37°C, 5% CO_2 with Control (Co), 2-Deoxy-D-Glucose (DG; 100mM; Sigma-Aldrich), Oligomycin (O; 1μM; Sigma-Aldrich) or a combination of both drugs (DGO). Puromycin (Puro, 10μg/ml; Sigma-Aldrich) is added for 15min at 37°C. SCENITH™ kit (http://www.scenith.com) containing all reagents and protocols were developed by Dr. Rafael Argüello, (CIML). Cells were washed in cold PBS and stained with primary conjugated antibodies against different surface markers (as described above) for 15min at 4°C in FACS buffer (PBS 1X 5% FCS, 2mM EDTA). After washing with FACS buffer, cells were fixed and permeabilized using Cytofix/Cytoperm™ (BD) following manufacturer's instructions. Intracellular staining of puromycin using the anti-Puro monoclonal antibody (1:600, Clone R4743L-E8) was performed by incubating cells during 30min at 4°C diluted in Permwash. Experimental duplicates were performed in all conditions.

In vivo glucose uptake

2-NBDG (300μg diluted in PBS 1X; Cayman chemical) was injected i.v. in C57Bl/6J mice; 15min later, cells from tumors were harvested.

Assessment of mitochondrial morphology

Mitochondrial membrane potential was measured using tetramethylrhodamine, ethyl ester (TMRE; 100nM; Abcam) according to manufacturer protocols. Following TMRE staining, carbonyl cyanide-4-(trifluoromethoxy) phenylhydrazone (FCCP; 25μM; Abcam) was used as a positive control for mitochondrial membrane depolarization. Total mitochondrial mass was assessed using MitoTracker Green (Invitrogen) according to manufacturer's instructions. All cells were subsequently analyzed by flow cytometry.

Triglyceride Quantification

Triglycerides (TAGs) were quantified from expanded γδ T cells *in vitro* using Picoprobe Triglyceride Quantification Assay Kit, Fluorometric (Abcam) and absorbance measured using FLUOstar OPTIMA (BMG Labtech).

RNA isolation and real-time PCR

mRNA was prepared from FACS-sorted $CD27^+$ and $CD27^-$ γδ T cells from WT spleen and draining lymph nodes using High Pure RNA Isolation kit (Roche). Reverse transcription was performed with random oligonucleotides (Invitrogen). Results were normalized to actin mRNA. qPCR was performed with SYBR Premix Ex Taq master mix (Takara) on an ABI ViiA7 cycler (Applied Biosystems). The CT for the target gene was subtracted from the CT for the endogenous reference, and the relative amount was calculated as $2^{-\Delta CT}$.

Imaging

Thymocytes from B6 E15 thymic lobes cultured for 12 days were isolated and stained for surface markers and then Mitotracker Green or TMRE (as described above). All cells were subsequently analyzed on an ImageStream™ Mark II imaging flow cytometer using INSPIRE acquisition software (Amnis); 30k events were saved from samples and 1k positive events from compensation single color controls. Analysis was performed using IDEAS® version 6.2.

For lipid droplet quantification, γδ T cells expanded *in vitro* were stained with LipidTOX red neutral lipid stain (Invitrogen) and Hoechst 33342 (Sigma-Aldrich). Mitotracker Green FM (Invitrogen) was used to identify mitochondria. Cells were mounted onto poly-L-lysine coated slides. Images were obtained with a Zeiss LSM 800 confocal microscope using Zen 2.3 software (Zeiss) and analyzed using ImageJ.

RNA-sequencing and data processing

Single-cell sequencing libraries were generated using the Chromium™ Single Cell 5' Library and Gel Bead Kit (10X Genomics) according to the manufacturer's instructions. Data was analyzed using the R package Seurat v2.3[55,56].

UMI counts were normalized using regularized negative binomial regression with the sctransform package[57]. For downstream analysis of normalized data principal component analysis (PCA) was performed using n=50 dimensions and PCA variability was determined using an Elbow plot. Differential gene expression analysis and GSEA was performed using the MAST and fgsea packages[56,57]. Pathways and gene lists for gene set enrichment analysis were obtained using the misgdbr package from Molecular Signatures database (MSigDB)[58,59]. Adaptively-thresholded Low Rank Approximation (ALRA) from the Seurat wrappers package was performed to correct for drop-out values for visualization of leading-edge and differentially expressed genes identified by MAST[60].

All downstream analysis was performed using R v.3.6.3 and RStudio Desktop 1.2.5001 on an Ubuntu 19.10 linux (64 bit) system using the following R packages and libraries: dplyr

v.0.8.5, fgsea v.1.12.0, ggplot2 v.3.3.0, MAST v.1.12.0, sctransform v.0.2.1, Seurat v.3.1.4, SeuratWrappers v.0.1.0, uwot v.0.1.8 and viridis v.0.5.1.

Statistical analysis

Statistical analysis was performed using GraphPad Prism software using non-parametric two-tailed Mann-Whitney test or, if both groups followed a normal distribution (tested by D'Agostino and Pearson normality test), using two-tailed unpaired Student *t* test or one-way analysis of variance. All data are presented as means ± standard error of mean (SEM) or standard deviation (SD). *$p < 0.05$; **$p < 0.01$; ***$p < 0.001$, ****<0.0001. Further information on research design is available in the Nature Research Reporting Summary linked to this article.

Europe PMC Funders Author Manuscripts

Europe PMC Funders Author Manuscripts

Extended Data

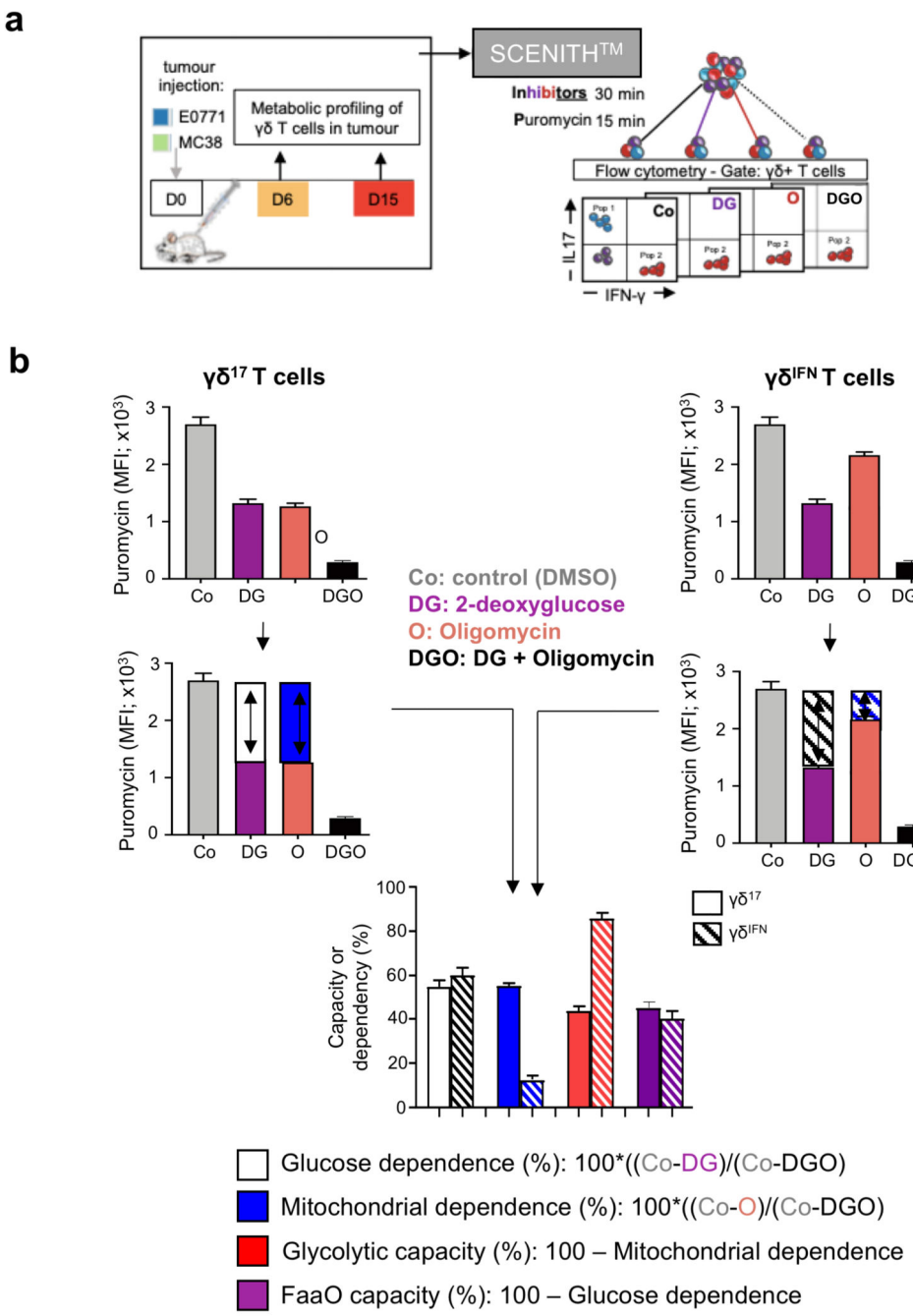

Extended Data Fig. 1. SCENITH™ methodology for analysis of cell metabolism

(a) Experimental design: E0771 breast or MC38 colon cancer cell lines were injected in WT mice; 6 and 15 days later, tumors were extracted for metabolic analysis of gd T cells using SCENITH™. **(b)** SCENITH™ assesses the impact of metabolic inhibitors on protein synthesis. Mean fluorescence intensity (MFI) of puromycin is analysed in each condition (Co: control-no inhibition; DG: 2-deoxyglucose inhibiting glycolysis; O: oligomycin

inhibiting OXPHOS; and DGO: DG+O inhibitors). Glucose dependence, fatty acid and amino acid oxidation capacity, mitochondrial dependence and glycolytic capacity are calculated as detailed in the Methods and reference #23. Error bars show mean + SEM. Data are representative of 3 independent experiments (n=3 mice in triplicates per group and per experiment).

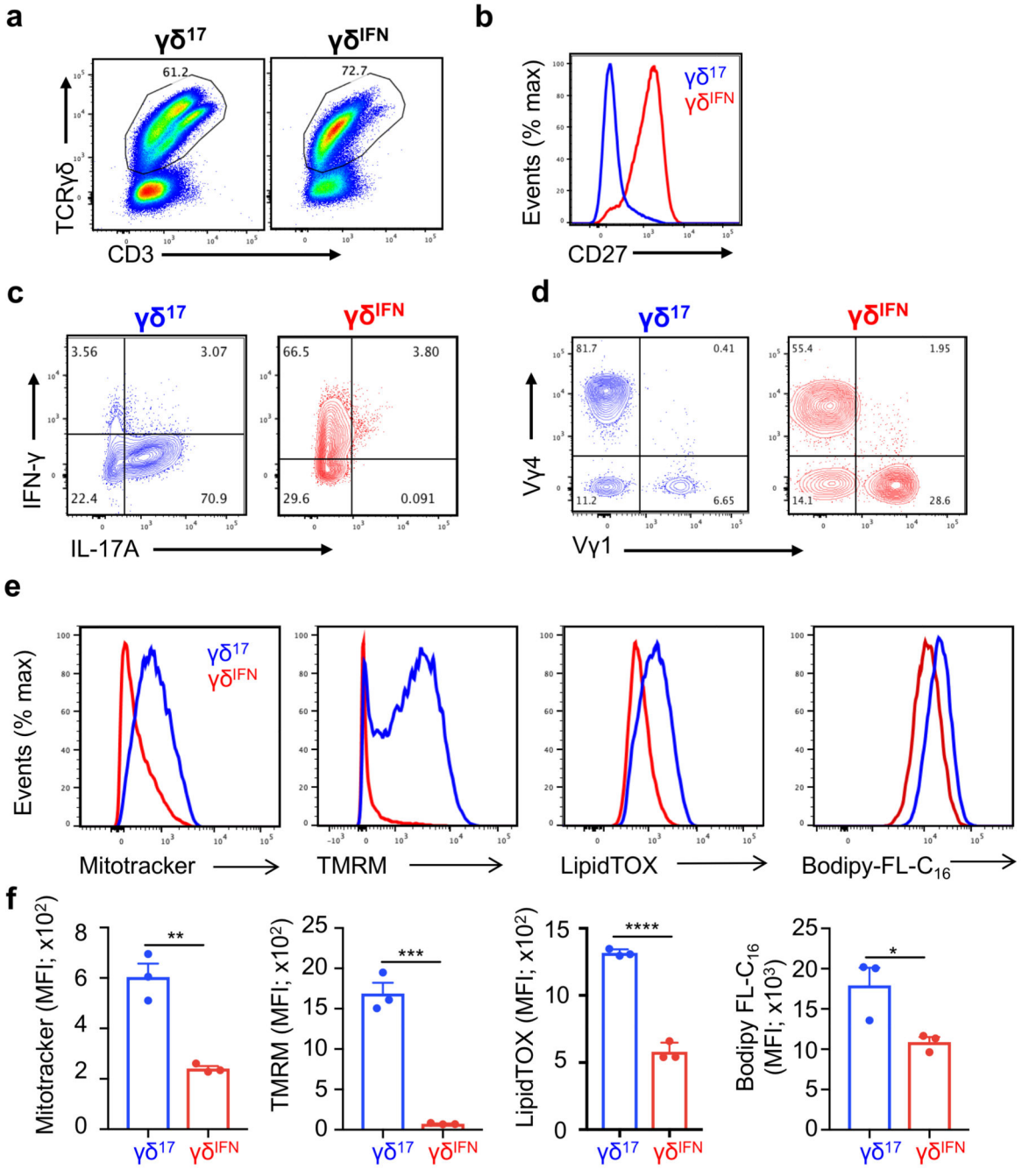

Extended Data Fig. 2. ***In vitro*** **expanded γδ^{17} and γδ^{IFN} γδ T cells retain their mitochondrial and lipid phenotypes.**

Europe PMC Funders Author Manuscripts

(a) Representative flow plots of CD3 and TCRγδ expression on $\gamma\delta^{17}$ and $\gamma\delta^{IFN}$ T cells expanded *in vitro* from total spleen/LN cells. **(b)** CD27 expression on *in vitro* expanded $\gamma\delta^{17}$ and $\gamma\delta^{IFN}$ γδ T cells. **(c)** IL-17 and IFNγ production by *in vitro* expanded $\gamma\delta^{17}$ and $\gamma\delta^{IFN}$ T cells respectively, following activation with PMA/ionomycin. **(d)** Vγ1 and Vγ4 expression on *in vitro* expanded $\gamma\delta^{17}$ and $\gamma\delta^{IFN}$ T cells. **(e)** Representative staining of *in vitro* expanded $\gamma\delta^{17}$ and $\gamma\delta^{IFN}$ T cells for mitotracker, TMRM, lipidTOX and Bodipy-FL-C_{16}. **(f)** MFI of mitotracker, TMRM, lipidTOX and Bodipy-FL-C_{16} staining *in vitro* expanded $\gamma\delta^{17}$ and $\gamma\delta^{IFN}$ T cells. n=3, data representative of 3 independent experiments. Mitotracker p=0.0026; TMRM p=0.0003; LipidTOX p<0.0001; Bodipy FL-C_{16} p=0.036. Error bars show mean + SD, **p < 0.01, ***p<0.001, ****p < 0.0001, using two-tailed unpaired Student's t-test.

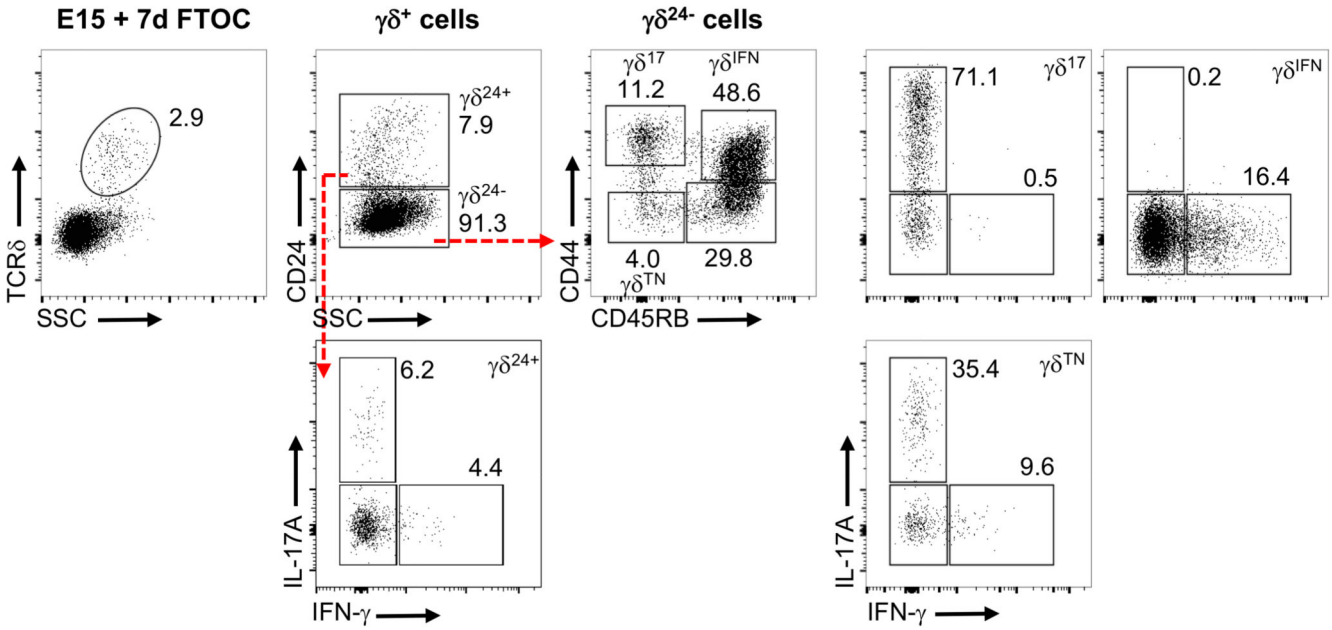

Extended Data Fig. 3. $\gamma\delta^{TN}$ cells can generate $\gamma\delta^{17}$ and $\gamma\delta^{IFN}$ T cells.

Flow cytometry profiles of thymic γδ T cells from E15 thymic lobes that had been cultured for 7-days in fetal thymic organ culture (E15 + 7dFTOC). $CD24^+$ ($\gamma\delta^{24+}$) precursors downregulate CD24 to become a $CD24^-CD44^-CD45RB^-$ ($\gamma\delta^{TN}$) population. $\gamma\delta^{TN}$ cells are able to become either IL-17-secreting $CD44^+CD45RB^-$ $\gamma\delta^{17}$ cells, or IFN-γ-producing $CD44^+CD45RB^+$ $\gamma\delta^{IFN}$ cells.

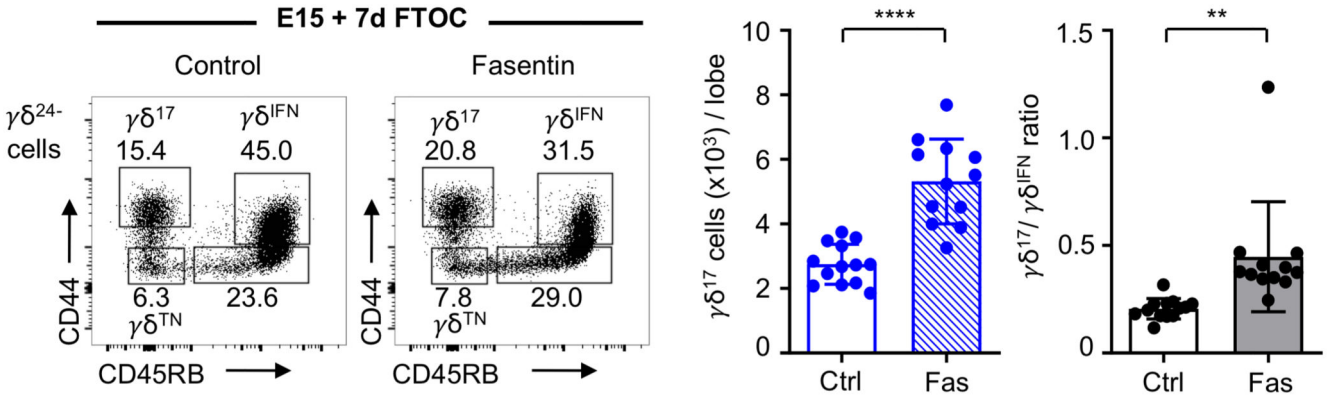

Extended Data Fig. 4. Thymic $\gamma\delta^{17}$ cells are increased upon inhibition of glucose uptake.

Flow cytometry profiles of thymic $\gamma\delta^{TN}$ ($CD44^{-}CD45RB^{-}$), $\gamma\delta^{17}$ ($CD44^{+}CD45RB^{-}$) and $\gamma\delta^{IFN}$ ($CD44^{+}CD45RB^{+}$) cells in $\gamma\delta^{24-}$ cells from E15 thymic lobes in 7-day FTOC with media containing or not Fasentin. Histograms show the number of $\gamma\delta^{17}$ T cells ($p<0.0001$) and $\gamma\delta^{17}/\gamma\delta^{IFN}$ ratio ($p=0.0028$). Data are representative of 2 independent experiments (at least 4 lobes pooled per group per experiment). Error bars show mean ± SEM, **p < 0.01, ****p < 0.0001, using two-tailed unpaired Student's t-test.

Europe PMC Funders Author Manuscripts

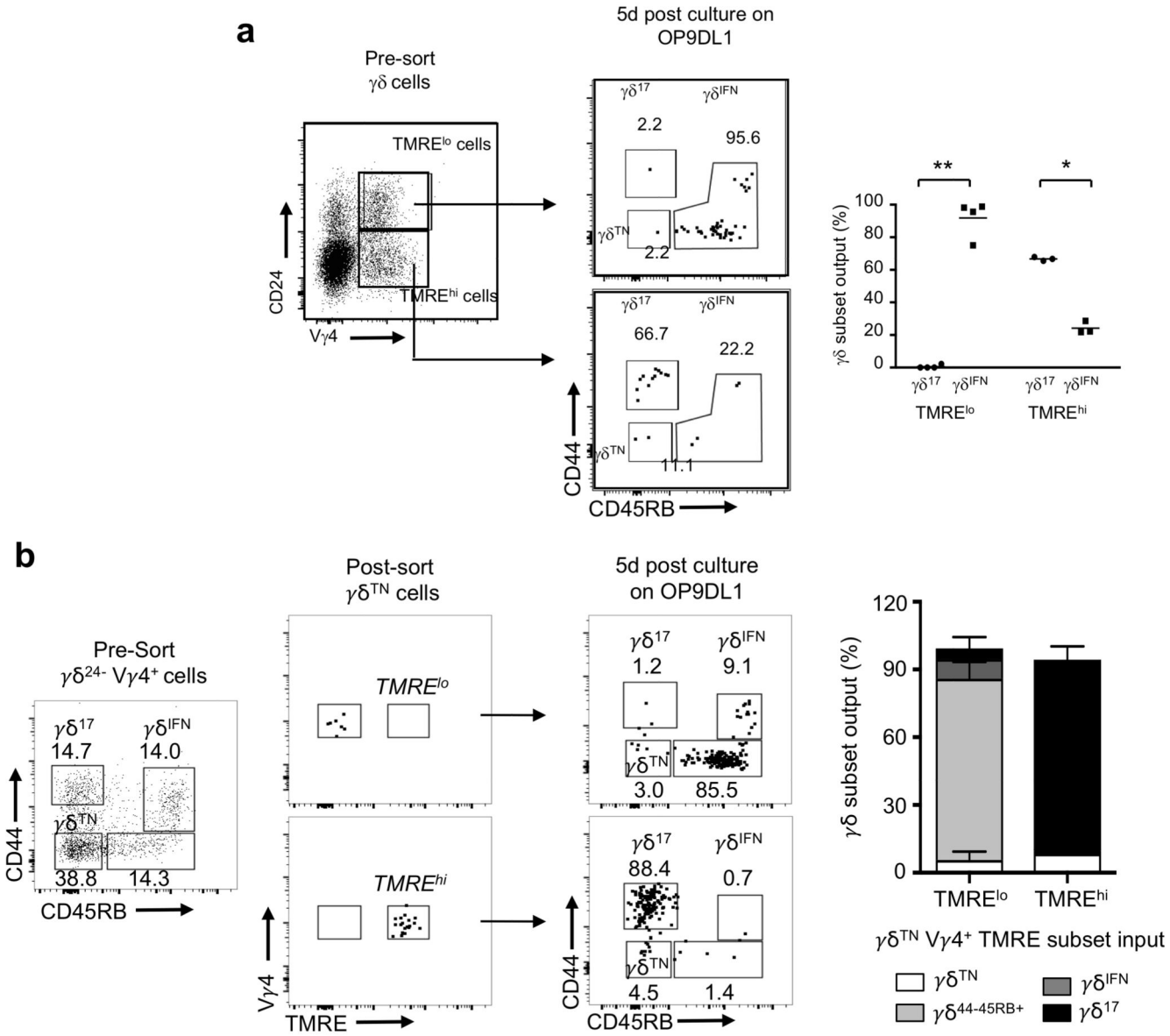

Extended Data Fig. 5. Mitochondrial activity identifies Vγ4$^+$ progenitors with distinct effector fates at very early stages.

(a) Flow cytometry plots pre-sort, and after sorted TMRE^{lo} and TMRE^{hi} Vγ4$^+$γδ24$^+$ cells were cultured for 5-days on OP9DL1 cells. Percentage of thymic γδ^{17} and γδ^{IFN} cells generated are displayed in the graph on right. Data are representative of 3 independent experiments (cells sorted from n = 4 independent mice pooled per group per experiment). **(b)** Flow cytometry plots for pre- and post-sort TMRE^{hi} and TMRE^{lo} Vγ4$^+$γδ^{TN} cells that were cultured on OP9-DL1 cells for a further 5-days (plots on right). Histogram shows the percentage of each γδ T cell subset generated from cultured TMRE^{lo} and TMRE^{hi} Vγ4$^+$γδ^{TN} cells. Error bars show mean + SD. Data are representative of 2 independent experiments (at least 4 lobes pooled per group per experiment). Error bars show mean ± SD, *p < 0.05, ***p < 0.01, using two-tailed unpaired Student's t-test.

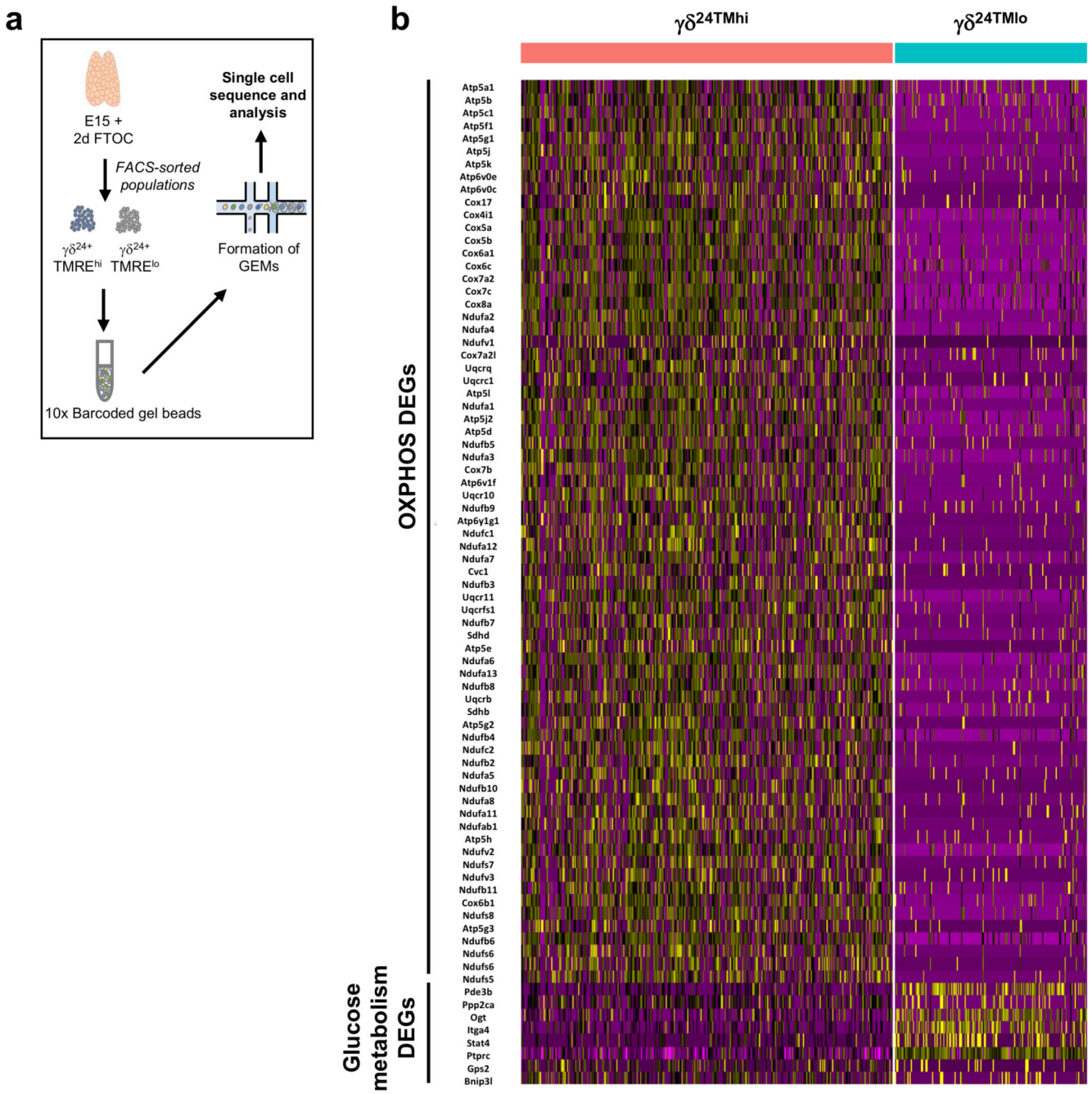

Extended Data Fig. 6. Distinct mitochondrial activities underlie effector fate of thymic γδ T cell progenitors.

(a) Experimental design for single-cell RNAseq (10x Genomics) on TMRE^{lo} and TMRE^{hi} gd^{24+} cells from E15 + 2d FTOC. **(b)** Heatmap of differentially upregulated genes from comparison of TMRE^{lo} and TMRE^{hi} gd^{24+} cells. Genes are grouped in relation to their function in either OxPhos or glucose metabolism.

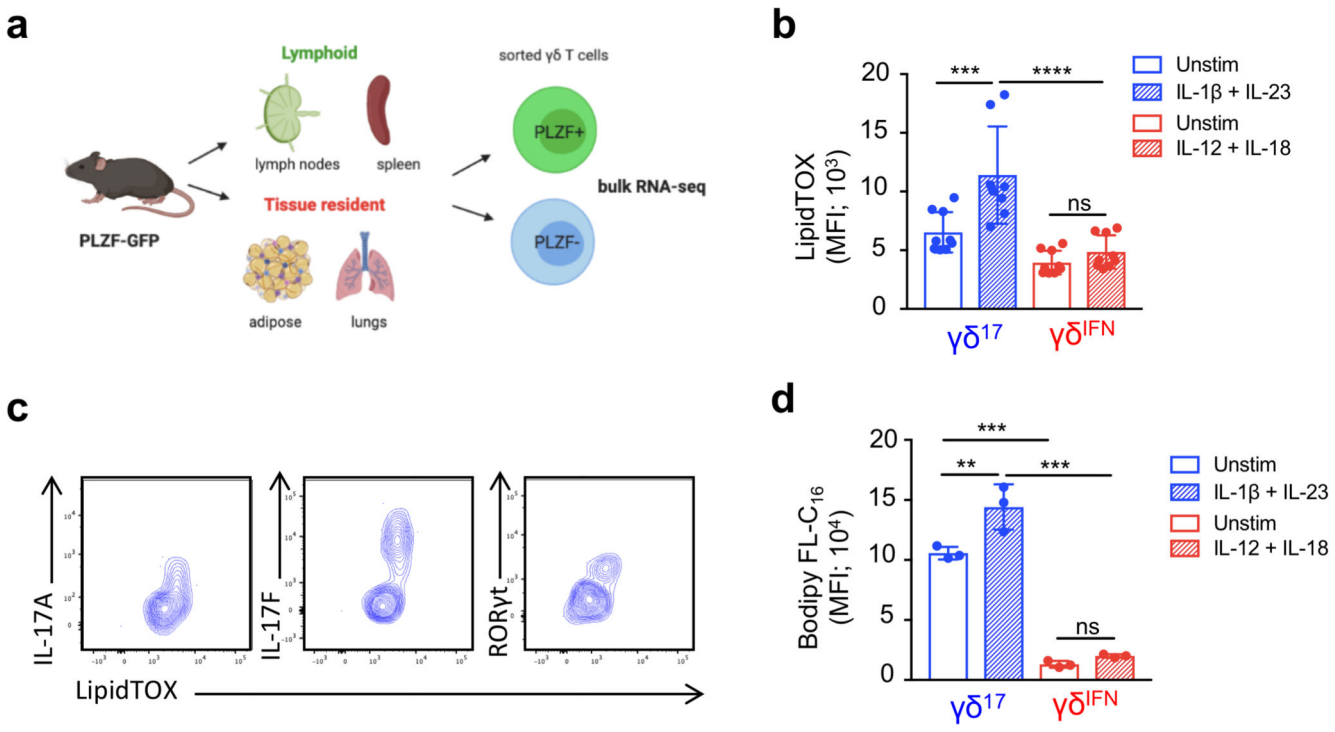

Extended Data Fig. 7. Enriched lipid metabolism and higher lipid uptake in γδ^{17} cells

(a) Experimental set up for bulk RNA-sequencing of PLZF^{+} (gd^{17}) and PLZF^{-} (gd^{IFN}) cells isolated from PLZF-GFP (*Zbtb16*^{GFP}) mice. **(b)** LipidTOX MFI in γδ^{17} (CD27^{-}) and γδ^{IFN} (CD27^{+}) T cells from LN cells activated *in vitro* with IL-1β+IL-23 and IL-12+IL-18 respectively. n=9, data pooled from 3 independent experiments. **(c)** Representative plots of LipidTOX staining and IL-17A, IL-17F or RORγt expression in γδ^{27-} T cells from LNs activated *in vitro* with IL-1β+IL-23 for 6h. Data representative of 3 independent experiments. **(d)** Bodipy-FL-C_{16} MFI in γδ^{17} (CD27^{-}) and γδ^{IFN} (CD27^{+}) T cells T cells unstimulated or stimulated *in vitro* with IL-12+IL-18 or IL-1β+IL-23.(n=3, data from 1 experiment; γδ^{17} p= 0.0044; γδ^{IFN} p=0.8035). Error bars show mean + SD, **p < 0.01, ***p < 0.001, ****p < 0.0001 using one-way ANOVA.

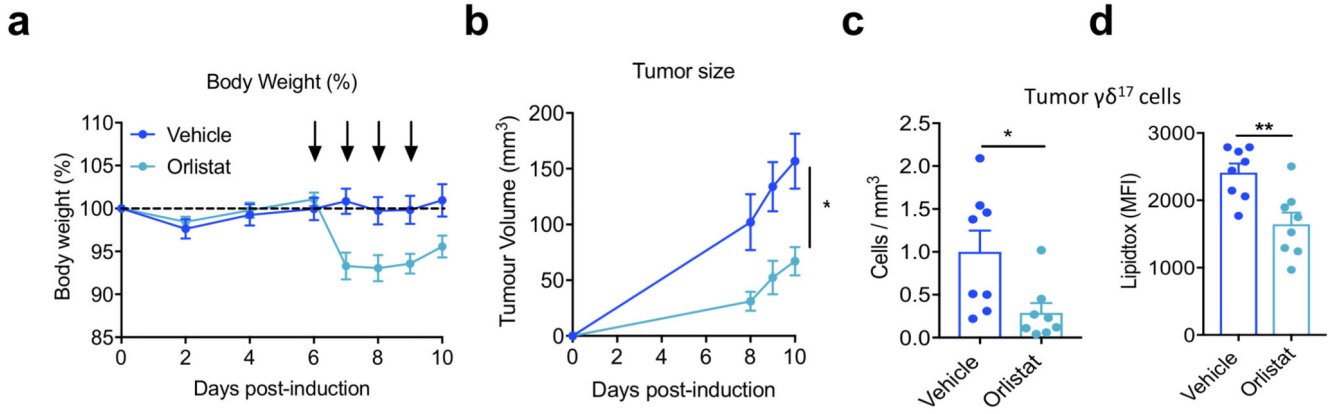

Extended Data Fig. 8. Inhibition of dietary fat uptake reduces tumour growth and γδ^{17} cells in the tumour.

B16F10-tumour bearing mice were given daily injections of either vehicle or orlistat on days 6-9, and tumours were analysed on day 10. **(a)** Percentage body weight following tumor cell injection; arrows indicate when orlistat or vehicle were administered. **(b)** Tumor volume on days 8-10 following B16F10 inoculation. Absolute numbers **(c)** and LipidTOX staining **(d)** of tumor-infiltrating γδ^{17} cells on day 10. n=8 biologically independent animals, data from 1 independent experiment. Data represents mean + SD, *p<0.06, **p < 0.01 using unpaired Student's t-test or one-way ANOVA.

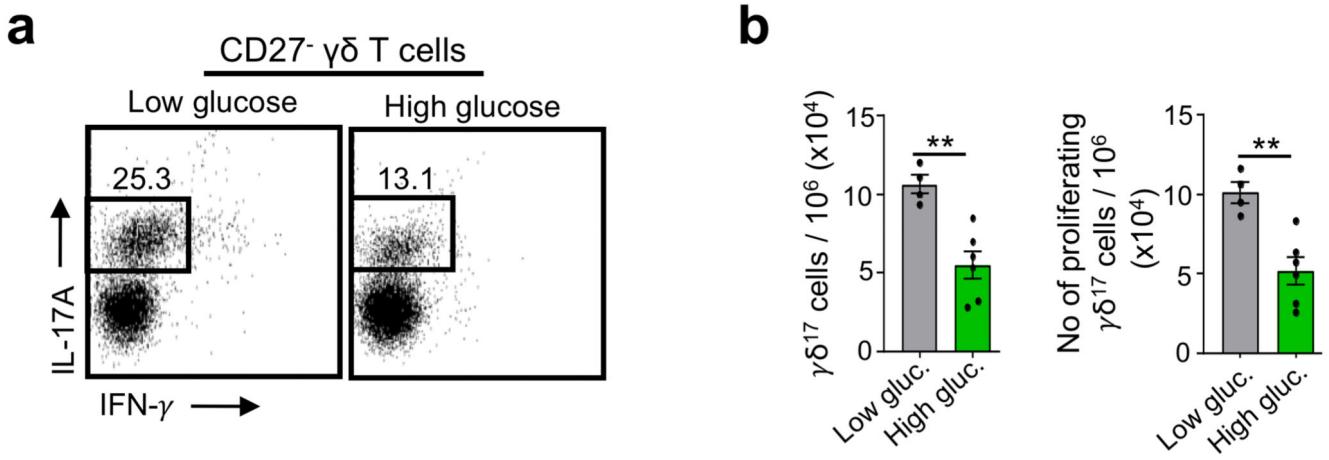

Extended Data Fig. 9. Glucose supplementation diminishes γδ^{17} cell numbers and proliferation.

(a) Flow cytometry profiles of peripheral γδ^{17} T cells cultured with media containing low (5mM) or high (50mM) doses of glucose. Graph depicts total numbers of γδ^{17} T cells (p=0.0028). **(b)** Number of proliferating Ki-67^{+} γδ^{17} T cells cultured with low or high glucose (p=0.0034). n=6 biologically independent animals, data from 2 independent experiments. Error bars show mean ± SEM, **p < 0.01, using unpaired two-tailed Student's t-test.

Supplementary Material

Refer to Web version on PubMed Central for supplementary material.

Acknowledgments

We are grateful for the valuable assistance of the staff of the flow cytometry, bioimaging and animal facilities at our Institutions. We thank J.-W. Taanman, A. Magalhães, J. Ribot, K. Serre, and N. Sousa for technical suggestions and administrative help. This work was supported by the Wellcome Trust (092973/Z/10/Z to D.J.P.), Biotechnology and Biological Sciences Research Council (BBSRC) UK (BB/R017808/1 to D.J.P.), European Research Council (CoG_646701 to B.S.-S.; StG_679173 to L.L.), Science Foundation Ireland (SFI) (16/FRL/3865 to L.L), NIH (NS115064, HG008155, AG062377 to M.K), R01 AI134861, Astrazeneca (Prémio FAZ Ciência 2019 to B.S.-S. and N.L.) and PAC-PRECISE LISBOA-01-0145-FEDER-016394, co-funded by FEDER (POR Lisboa 2020) and Fundação para a Ciência e a Tecnologia (Portugal). N.L is supported by a post-doctoral fellowship from EMBO (ALTF 752-2018); S.M. was supported by a studentship from the Medical Research Council (MRC) UK; G.F. is supported by a European Commission Marie Sklodowska-Curie Individual Fellowship (ref. 752932); and A.D, S.C. L.D and H.P are supported by Irish Research Council fellowships.

Europe PMC Funders Author Manuscripts

Data Availability

The GEO public repository accession codes are; GSE150585 for single-cell RNA sequencing; and GSE156782 for bulk RNA sequencing. The data that support the findings of this study are available from the corresponding author upon request.

References

1. Buck MD, Sowell RT, Kaech SM, Pearce EL. Metabolic Instruction of Immunity. Cell. 2017; 169:570–586. DOI: 10.1016/j.cell.2017.04.004 [PubMed: 28475890]
2. Almeida L, Lochner M, Berod L, Sparwasser T. Metabolic pathways in T cell activation and lineage differentiation. Semin Immunol. 2016; 28:514–524. DOI: 10.1016/j.smim.2016.10.009 [PubMed: 27825556]
3. Geltink RIK, Kyle RL, Pearce EL. Unraveling the Complex Interplay Between T Cell Metabolism and Function. Annu Rev Immunol. 2018; 36:488–488. DOI: 10.1146/annurev-immunol-042617-053019
4. Cham CM, Driessens G, O'Keefe JP, Gajewski TF. Glucose deprivation inhibits multiple key gene expression events and effector functions in CD8+ T cells. Eur J Immunol. 2008; 38:2450–2450. DOI: 10.1002/eji.200838289
5. Chang CH, et al. Posttranscriptional control of T cell effector function by aerobic glycolysis. Cell. 2013; 153:1251–1251. DOI: 10.1016/j.cell.2013.05.016
6. Chang CH, et al. Metabolic Competition in the Tumor Microenvironment Is a Driver of Cancer Progression. Cell. 2015; 162:1241–1241. DOI: 10.1016/j.cell.2015.08.016
7. O'Sullivan D, Sanin DE, Pearce EJ, Pearce EL. Metabolic interventions in the immune response to cancer. Nat Rev Immunol. 2019; 19:335–335. DOI: 10.1038/s41577-019-0140-9
8. Silva-Santos B, Mensurado S, Coffelt SB. gammadelta T cells: pleiotropic immune effectors with therapeutic potential in cancer. Nat Rev Cancer. 2019; 19:404–404. DOI: 10.1038/s41568-019-0153-5
9. Sebestyen Z, Prinz I, Dechanet-Merville J, Silva-Santos B, Kuball J. Translating gammadelta (gammadelta) T cells and their receptors into cancer cell therapies. Nat Rev Drug Discov. 2020; 19:184–184. DOI: 10.1038/s41573-019-0038-z
10. Chien YH, Meyer C, Bonneville M. gammadelta T cells: first line of defense and beyond. Annu Rev Immunol. 2014; 32:155–155. DOI: 10.1146/annurev-immunol-032713-120216
11. Hayday AC. Gammadelta T cells and the lymphoid stress-surveillance response. Immunity. 2009; 31:196–196. DOI: 10.1016/j.immuni.2009.08.006
12. Hayday AC. gammadelta T Cell Update: Adaptate Orchestrators of Immune Surveillance. J Immunol. 2019; 203:320–320. DOI: 10.4049/jimmunol.1800934
13. Ravens S, et al. Human gammadelta T cells are quickly reconstituted after stem-cell transplantation and show adaptive clonal expansion in response to viral infection. Nat Immunol. 2017; 18:401–401. DOI: 10.1038/ni.3686
14. Kohlgruber AC, et al. gammadelta T cells producing interleukin-17A regulate adipose regulatory T cell homeostasis and thermogenesis. Nat Immunol. 2018; 19:474–474. DOI: 10.1038/s41590-018-0094-2
15. Ribeiro M, et al. Meningeal gammadelta T cell-derived IL-17 controls synaptic plasticity and short-term memory. Sci Immunol. 2019; 4doi: 10.1126/sciimmunol.aay5199
16. Papotto PH, Ribot JC, Silva-Santos B. IL-17(+) gammadelta T cells as kick-starters of inflammation. Nat Immunol. 2017; 18:611–611. DOI: 10.1038/ni.3726
17. Jensen KD, et al. Thymic selection determines gammadelta T cell effector fate: antigen-naive cells make interleukin-17 and antigen-experienced cells make interferon gamma. Immunity. 2008; 29:100–100. DOI: 10.1016/j.immuni.2008.04.022
18. Ribot JC, et al. CD27 is a thymic determinant of the balance between interferon-gamma- and interleukin 17-producing gammadelta T cell subsets. Nat Immunol. 2009; 10:436–436. DOI: 10.1038/ni.1717

19. Sumaria N, Grandjean CL, Silva-Santos B, Pennington DJ. Strong TCRgammadelta Signaling Prohibits Thymic Development of IL-17A-Secreting gammadelta T Cells. Cell Rep. 2017; 19:2476–2476. DOI: 10.1016/j.celrep.2017.05.071
20. Munoz-Ruiz M, et al. TCR signal strength controls thymic differentiation of discrete proinflammatory gammadelta T cell subsets. Nat Immunol. 2016; 17:727–727. DOI: 10.1038/ni.3424
21. Munoz-Ruiz M, Sumaria N, Pennington DJ, Silva-Santos B. Thymic Determinants of gammadelta T Cell Differentiation. Trends Immunol. 2017; 38:344–344. DOI: 10.1016/j.it.2017.01.007
22. Silva-Santos B, Serre K, Norell H. gammadelta T cells in cancer. Nat Rev Immunol. 2015; 15:691–691. DOI: 10.1038/nri3904
23. Argüello R, Combes AJ, Char R, Gigan JP, Baaziz AI, Bousiquot E, Camosseto V, Samad B, Tsui J, Yan P, Boissoneau S, Figarella-Branger D, et al. SCENITH: A flow cytometry based method for functional profiling energy metabolism with single cell resolution. Cell Metabolism (in Press). 2020
24. Gleyzer N, Vercauteren K, Scarpulla RC. Control of mitochondrial transcription specificity factors (TFB1M and TFB2M) by nuclear respiratory factors (NRF-1 and NRF-2) and PGC-1 family coactivators. Mol Cell Biol. 2005; 25:1366–1366. DOI: 10.1128/MCB.25.4.1354-1366.2005
25. Scarpulla RC. Nuclear control of respiratory chain expression in mammalian cells. J Bioenerg Biomembr. 1997; 29:119–119. DOI: 10.1023/a:1022681828846
26. Dang CV, et al. The c-Myc target gene network. Semin Cancer Biol. 2006; 16:264–264. DOI: 10.1016/j.semcancer.2006.07.014
27. Guo QM, et al. Identification of c-myc responsive genes using rat cDNA microarray. Cancer Res. 2000; 60:5922–5928. [PubMed: 11085504]
28. In TSH, et al. HEB is required for the specification of fetal IL-17-producing gammadelta T cells. Nat Commun. 2004; 8doi: 10.1038/s41467-017-02225-5(2017)
29. Coffey F, et al. The TCR ligand-inducible expression of CD73 marks gammadelta lineage commitment and a metastable intermediate in effector specification. J Exp Med. 2014; 211:343–343. DOI: 10.1084/jem.20131540
30. Turchinovich G, Hayday AC. Skint-1 identifies a common molecular mechanism for the development of interferon-gamma-secreting versus interleukin-17-secreting gammadelta T cells. Immunity. 2011; 35:68–68. DOI: 10.1016/j.immuni.2011.04.018
31. Lu Y, Cao X, Zhang X, Kovalovsky D. PLZF Controls the Development of Fetal-Derived IL-17+Vgamma6+ gammadelta T Cells. J Immunol. 2015; 195:4281–4281. DOI: 10.4049/jimmunol.1500939
32. Tan L, et al. Single-Cell Transcriptomics Identifies the Adaptation of Scart1(+) Vgamma6(+) T Cells to Skin Residency as Activated Effector Cells. Cell Rep. 2019; 27:3657–3671.e3654 DOI: 10.1016/j.celrep.2019.05.064 [PubMed: 31216482]
33. McCully ML, et al. Skin Metabolites Define a New Paradigm in the Localization of Skin Tropic Memory T Cells. J Immunol. 2015; 195:104–104. DOI: 10.4049/jimmunol.1402961
34. Bartz R, et al. Lipidomics reveals that adiposomes store ether lipids and mediate phospholipid traffic. J Lipid Res. 2007; 48:847–847. DOI: 10.1194/jlr.M600413-JLR200
35. Le Goffe C, Vallette G, Jarry A, Bou-Hanna C, Laboisse CL. The in vitro manipulation of carbohydrate metabolism: a new strategy for deciphering the cellular defence mechanisms against nitric oxide attack. Biochem J. 1999; 344(Pt 3):643–648. DOI: 10.1042/0264-6021:3440643 [PubMed: 10585850]
36. Bustamante E, Pedersen PL. High aerobic glycolysis of rat hepatoma cells in culture: role of mitochondrial hexokinase. Proc Natl Acad Sci U S A. 1977; 74:3739–3739. DOI: 10.1073/pnas.74.9.3735
37. Buck MD, O'Sullivan D, Pearce EL. T cell metabolism drives immunity. J Exp Med. 2015; 212:1360–1360. DOI: 10.1084/jem.20151159
38. Menk AV, et al. Early TCR Signaling Induces Rapid Aerobic Glycolysis Enabling Distinct Acute T Cell Effector Functions. Cell Rep. 2018; 22:1521–1521. DOI: 10.1016/j.celrep.2018.01.040

39. Shin B, et al. Mitochondrial Oxidative Phosphorylation Regulates the Fate Decision between Pathogenic Th17 and Regulatory T Cells. Cell Rep. 2020; 30:1898–1909.e1894 DOI: 10.1016/j.celrep.2020.01.022 [PubMed: 32049019]
40. Di Luccia B, Gilfillan S, Cella M, Colonna M, Huang SC. ILC3s integrate glycolysis and mitochondrial production of reactive oxygen species to fulfill activation demands. J Exp Med. 2019; 216:2241–2241. DOI: 10.1084/jem.20180549
41. Schmolka N, et al. Epigenetic and transcriptional signatures of stable versus plastic differentiation of proinflammatory gammadelta T cell subsets. Nat Immunol. 2013; 14:1100–1100. DOI: 10.1038/ni.2702
42. Schmolka N, Wencker M, Hayday AC, Silva-Santos B. Epigenetic and transcriptional regulation of gammadelta T cell differentiation: Programming cells for responses in time and space. Semin Immunol. 2015; 27:25–25. DOI: 10.1016/j.smim.2015.01.001
43. Gentles AJ, et al. The prognostic landscape of genes and infiltrating immune cells across human cancers. Nat Med. 2015; 21:945–945. DOI: 10.1038/nm.3909
44. Legut M, Cole DK, Sewell AK. The promise of gammadelta T cells and the gammadelta T cell receptor for cancer immunotherapy. Cell Mol Immunol. 2015; 12:668–668. DOI: 10.1038/cmi.2015.28
45. Nakamizo S, et al. High fat diet exacerbates murine psoriatic dermatitis by increasing the number of IL-17-producing gammadelta T cells. Sci Rep. 2017; 714076doi: 10.1038/s41598-017-14292-1 [PubMed: 29074858]
46. Goldberg EL, et al. Ketogenic diet activates protective gammadelta T cell responses against influenza virus infection. Sci Immunol. 2019; 4doi: 10.1126/sciimmunol.aav2026
47. Michelet X, et al. Metabolic reprogramming of natural killer cells in obesity limits antitumor responses. Nat Immunol. 2018; 19:1340–1340. DOI: 10.1038/s41590-018-0251-7
48. Fischer K, et al. Inhibitory effect of tumor cell-derived lactic acid on human T cells. Blood. 2007; 109:3819–3819. DOI: 10.1182/blood-2006-07-035972
49. Wang Z, et al. Glycolysis and Oxidative Phosphorylation Play Critical Roles in Natural Killer Cell Receptor-Mediated Natural Killer Cell Functions. Front Immunol. 2020; 11:202.doi: 10.3389/fimmu.2020.00202 [PubMed: 32153568]
50. Almeida AR, et al. Delta One T Cells for Immunotherapy of Chronic Lymphocytic Leukemia: Clinical-Grade Expansion/Differentiation and Preclinical Proof of Concept. Clin Cancer Res. 2016; 22:5804–5804. DOI: 10.1158/1078-0432.CCR-16-0597
51. Lynch L, et al. Regulatory iNKT cells lack expression of the transcription factor PLZF and control the homeostasis of T reg cells and macrophages in adipose tissue. Nat Immunol. 2015; 16:85–95. [PubMed: 25436972]
52. Vu JP, et al. Long-Term Intake of a High-Protein Diet Affects Body Phenotype, Metabolism, and Plasma Hormones in Mice. J Nutr. 2017; 147:2243–2251. [PubMed: 29070713]
53. Kohlgruber AC, et al. γδ T cells producing interleukin-17A regulate adipose regulatory T cell homeostasis and thermogenesis. Nat Immunol. 2018; 19
54. McKenzie DR, et al. IL-17-producing γδ T cells switch migratory patterns between resting and activated states. Nat Commun. 2017; 8:15632. [PubMed: 28580944]
55. Butler A, Hoffman P, Smibert P, Papalexi E, Satija R. Integrating single-cell transcriptomic data across different conditions, technologies, and species. Nat Biotechnol. 2018; 36:411–420. [PubMed: 29608179]
56. Stuart T, et al. Comprehensive Integration of Single-Cell Data Resource Comprehensive Integration of Single-Cell Data. Cell. 2019; 177
57. Hafemeister C, Satija R. Normalization and variance stabilization of single-cell RNA-seq data using regularized negative binomial regression. Genome Biol. 2019; 20:296. [PubMed: 31870423]
58. Subramanian A, et al. Gene set enrichment analysis: A knowledge-based approach for interpreting genome-wide expression profiles. Proc Natl Acad Sci U S A. 2005; 102:15545–15550. [PubMed: 16199517]
59. Liberzon A, et al. Databases and ontologies Molecular signatures database (MSigDB) 3.0. Bioinforma Appl NOTE. 2011; 27:1739–1740.

60. Linderman GC, Zhao J, Kluger Y. Zero-preserving imputation of scRNA-seq data using low-rank approximation. bioRxiv. 2018; 397588doi: 10.1101/397588

Europe PMC Funders Author Manuscripts

Europe PMC Funders Author Manuscripts

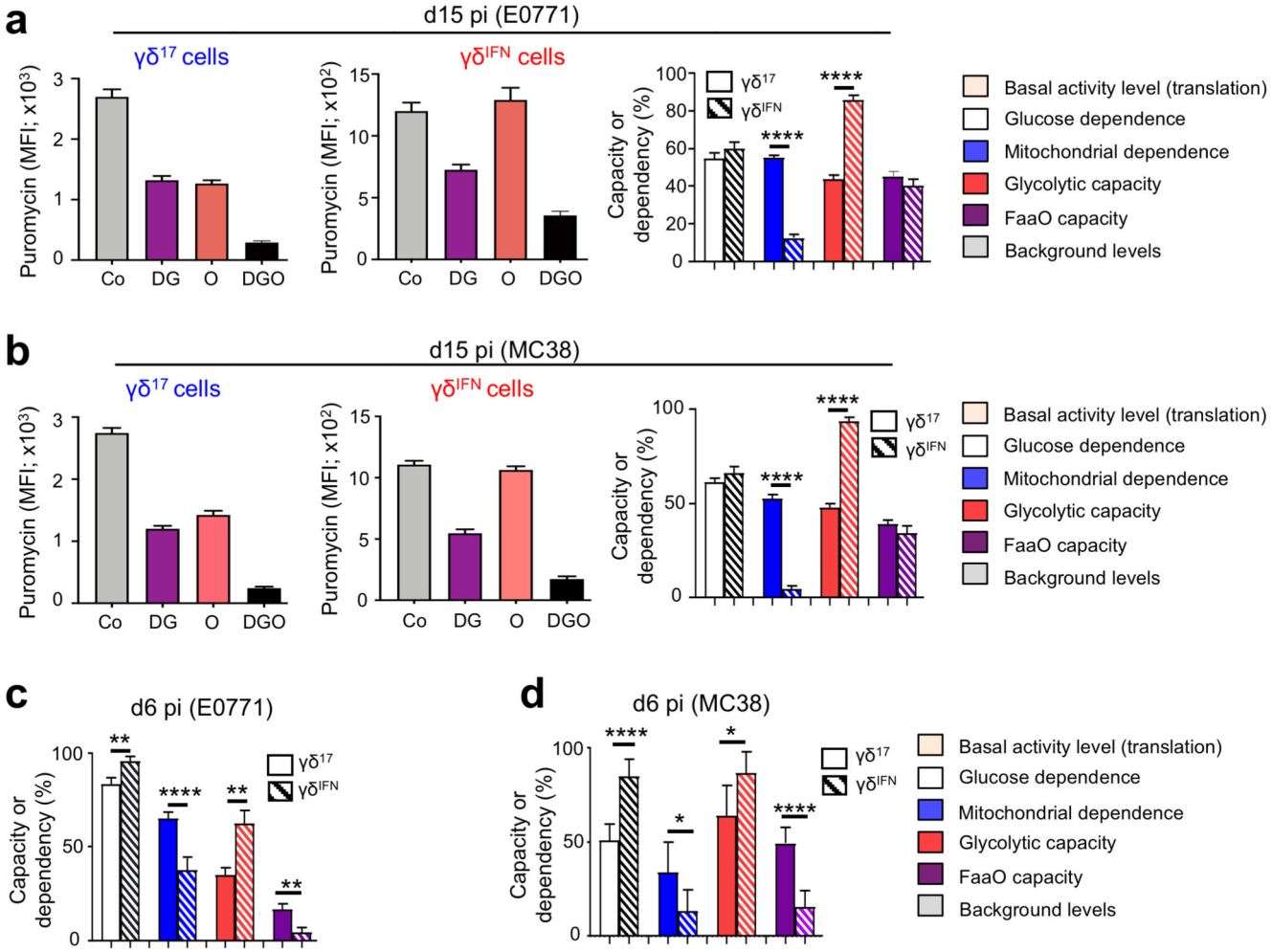

Figure 1. Intra-tumoral γδ T cell subsets display distinct metabolic profiles.

(a-d) Puromycin MFI of tumour-infiltrating γδ^{17} and γδ^{IFN} T cells extracted from E0771 breast **(a,c)** and MC38 colon **(b,d)** tumor-bearing mice analysed using SCENITH™ in; control conditions (Co), or after the addition of 2-deoxy-D-glucose (DG), oligomycin (O) or both inhibitors (DGO). Graphs show the percentage of glucose dependence, mitochondrial dependence, glycolytic capacity and fatty acid and amino acid oxidation (FaaO) capacity of tumor-infiltrating γδ^{17} and γδ^{IFN} cells isolated either 6-days (**c**: glucose dependence (p=0.0041), mitochondrial dependence (p<0.0001), glycolytic capacity (p=0.0014) and FaaO (p=0.0041); **d**: glucose dependence (p<0.0001), mitochondrial dependence (p=0.0345), glycolytic capacity (p=0.0189) and FaaO (p<0.0001)) or 15-days (**a,b**: mitochondrial dependence (p<0.0001), glycolytic capacity (p<0.0001)), after cancer cell line injection. Data are representative of three independent experiments (n=3 mice per group in triplicates in each experiment). pi: post-injection. γδ^{17} and γδ^{IFN} T cells represents IL-17 and IFN-γ-producing γδ T cells, respectively. Error bars show mean ± SEM, *p < 0.05; **p < 0.01; ****<0.0001 using unpaired two-tailed Student's t-test.

Europe PMC Funders Author Manuscripts

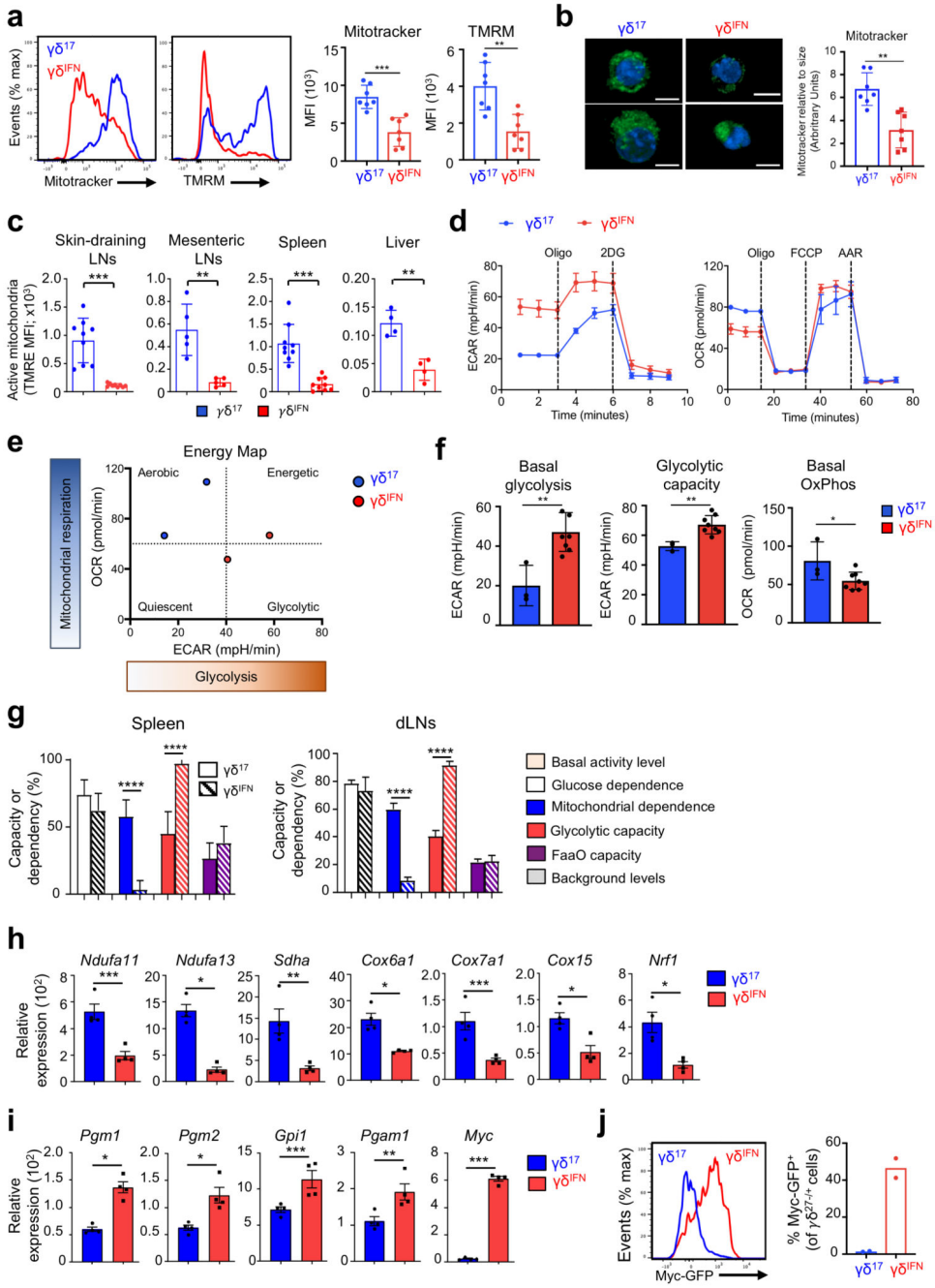

Figure 2. Peripheral γδ T cell subsets show different mitochondrial and metabolic phenotypes.

(a) Representative plots (left) and summary graphs (right) of the MFI of mitotracker and tetramethylrhodamine methyl ester (TMRM) in $\gamma\delta^{27-}$ ($\gamma\delta^{17}$) and $\gamma\delta^{27+}$ ($\gamma\delta^{IFN}$) T cells *ex vivo* from LNs of C57BL/6 mice (n=7; data pooled from 2 experiments; Mitotracker p=0.0003; TMRM p=0.0015). **(b)** Representative confocal images (left) of $\gamma\delta^{17}$ and $\gamma\delta^{IFN}$ T cells stained with mitotracker (green) and Hoechst 33342 (blue). Scale bar represents 5μM. Analysis of mitotracker staining relative to cell size (right) in $\gamma\delta^{17}$ and $\gamma\delta^{IFN}$ cells *ex vivo*. Relative mitotracker was calculated by dividing the MFI of mitotracker by the MFI of

FSC-A and multiplying by 100 (n=7, data pooled from 2 independent experiments; p=0.0012). **(c)** Tetramethylrhodamine ethyl ester (TMRE) MFI of $\gamma\delta^{17}$ and $\gamma\delta^{IFN}$ T cells from skin draining LNs, mesenteric LNs, spleen and liver of WT mice. Data are representative of 3 independent experiments (n=3 mice per group and experiment; sdLN p=0.0003; mLN p=0.0095; spleen p=0.0001; liver p=0.0016). **(d)** Seahorse extracellular flux analysis of extracellular acidification rate (ECAR) and oxygen consumption rate (OCR) of $\gamma\delta^{17}$ and $\gamma\delta^{IFN}$ T cells (expanded *in vitro*) from LNs ($\gamma\delta^{17}$ n=2, $\gamma\delta^{IFN}$ n=5, data representative of 3 independent experiments). **(e)** Energy map showing ECAR vs OCR of $\gamma\delta^{17}$ and $\gamma\delta^{IFN}$ T cells. Each symbol represents average basal metabolism. **(f)** Basal glycolytic rate, glycolytic capacity and basal OxPhos of $\gamma\delta^{17}$ (n=3) and $\gamma\delta^{IFN}$ (n=8) cell subsets (data pooled from 2 independent experiments; basal glycolysis p=0.0029; glycolytic capacity p=0.0042; basal OxPhos p=0.0339). **(g)** Percentage of glucose dependence, mitochondrial dependence, glycolytic capacity and fatty acid and amino acid oxidation (FaaO) capacity of $\gamma\delta^{17}$ and $\gamma\delta^{IFN}$ cells from spleen and draining lymph nodes (dLNs). Data are representative of 3 independent experiments (n=3 mice in triplicates per group and per experiment). **(h,i)** OxPhos-related genes (*Ndufa11*, p=0.0009*; Ndufa13*, p=0.0214; *Sdha*, p=0.0027*; Cox6a1*, p=0.0235; *Cox7a1*, p=0.0002*; Cox15*, p=0.0204; *Nrf1*, p=0.0248) and glycolysis-related genes (*Pgm1*, p=0.0226; *Pgm2*, p=0.0514; *Gpi1*, p=0.0003; *Pgam1*, p=0.0018; *Myc*, p=0.0002) were measured by qPCR in purified $\gamma\delta^{17}$ (n=4) and $\gamma\delta^{IFN}$ (n=4) cells from spleen and dLN from WT mice. **(j)** Representative plot (left) and percentages (right) of Myc-GFP+ $\gamma\delta^{17}$ and $\gamma\delta^{IFN}$ cells from LNs of Myc-GFP reporter mice (n=2). Error bars show mean ± SEM or SD, *p < 0.05; **p < 0.01; ***p < 0.001, ****<0.0001 using unpaired two-tailed Student's t-test.

Europe PMC Funders Author Manuscripts

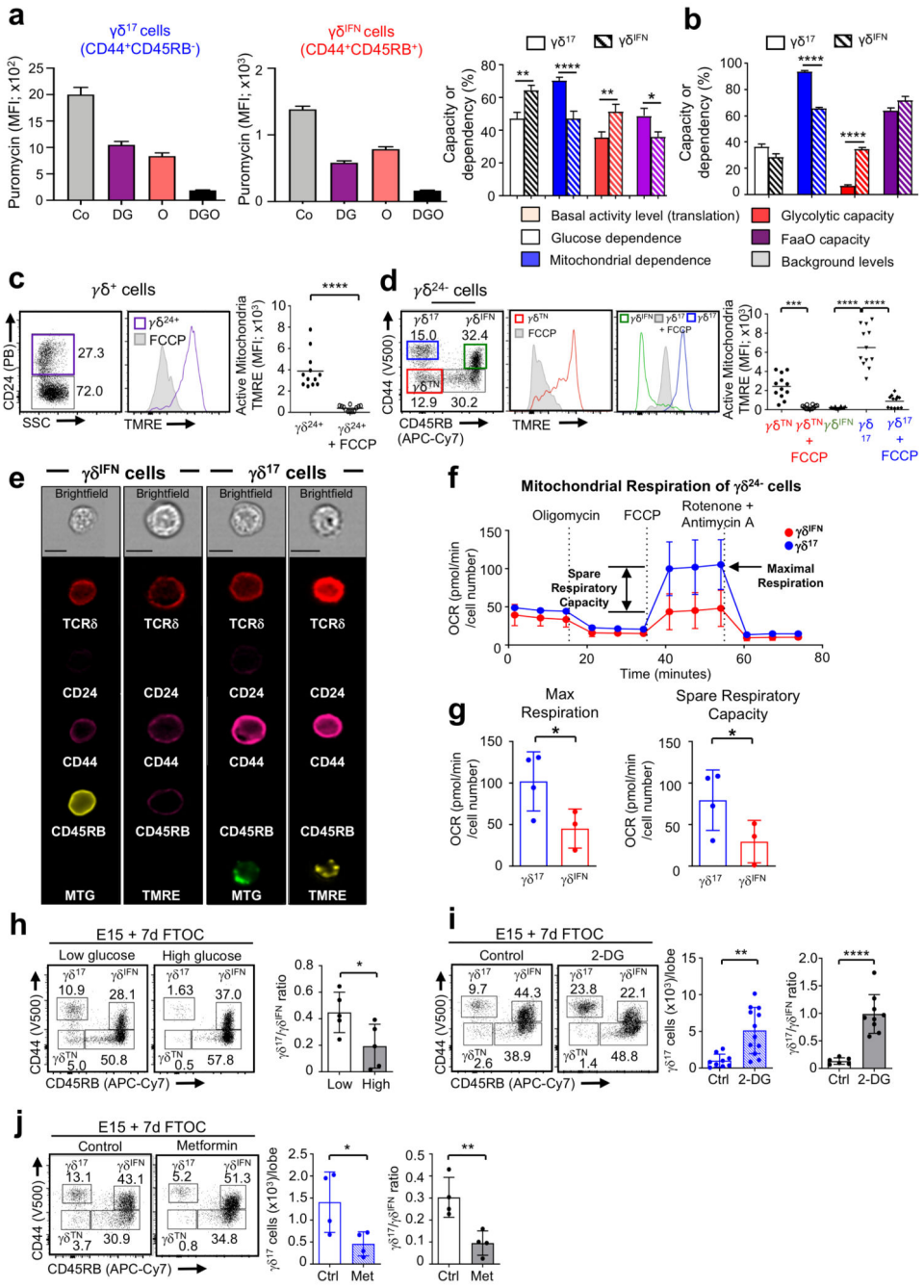

Figure 3. γδ T cell subsets are metabolically programmed in the thymus.

(a) Puromycin MFI of γδ^{17} (CD44^{hi}CD45RB^{-}) and γδ^{IFN} (CD44^{+}CD45RB^{+}) T cells from WT adult thymus in resting conditions (Co) and after the addition of 2-deoxy-D-glucose (DG), oligomycin (O) or both (DGO). Histogram (right) shows the percentage of glucose dependency (white; p=0.0029), mitochondrial dependency (blue; p<0.0001), glycolytic capacity (red, p=0.0018) and fatty acid and amino acid oxidation (FaaO) capacity (purple, p=0.0304) of thymic γδ^{17} and γδ^{IFN} cells. Data are representative of two independent experiments (n=5 mice in triplicates per group and per experiment). **(b)** Histograms shows

the percentage of glucose dependency (white), mitochondrial dependency (blue; $p<0.0001$), glycolytic capacity (red; $p<0.0001$) and fatty acid and amino acid oxidation (FaaO) capacity (purple) of $\gamma\delta^{17}$ and $\gamma\delta^{IFN}$ T cells from WT newborn thymus (d3). Data are representative of three independent experiments (n=6 mice in triplicates per group and per experiment). **(c)** Flow cytometry profile and Tetramethylrhodamine ethyl ester (TMRE) MFI of thymic $\gamma\delta^{24+}$ precursors treated or not with FCCP ($p<0.0001$). Data are representative of 3 independent experiments (data points represent at least 4 lobes pooled per group and per experiment). **(d)** Flow cytometry profiles and TMRE MFI of thymic $\gamma\delta^{TN}$ ($CD44^{-}CD45RB^{-}$), $\gamma\delta^{17}$ ($CD44^{hi}CD45RB^{-}$) and $\gamma\delta^{IFN}$ ($CD44^{+}CD45RB^{+}$) cells treated or not with FCCP. $\gamma\delta^{TN}$ vs $\gamma\delta^{TN}$+FCCP ($p=0.0002$), $\gamma\delta^{IFN}$ vs $\gamma\delta^{17}$ ($p<0.0001$), and $\gamma\delta^{17}$ vs $\gamma\delta^{17}$+FCCP ($p<0.0001$). Data are representative of 3 independent experiments (data points represent at least 4 lobes pooled per group and per experiment). **(e)** Imagestream analysis of $\gamma\delta^{17}$ and $\gamma\delta^{IFN}$ cells stained with either mitotracker green or TMRE. Scale bar represents 7μm. Data are representative of 2 independent experiments. **(f)** O_2 consumption rates (OCR) of $\gamma\delta^{17}$ and $\gamma\delta^{IFN}$ cells from thymuses of 5-day old B6 pups were measured by Seahorse extracellular flux analysis in real-time under basal conditions and in response to indicated mitochondrial inhibitors. Data are representative of 3 independent experiments (pooled thymic lobes from n>10 mice per group per experiment). **(g)** Histograms show maximal respiration potential ($p=0.0278$) and spare respiratory capacity ($p=0.0332$) by measuring oxygen consumption rates (OCR) of $\gamma\delta^{17}$ and $\gamma\delta^{IFN}$ cells from thymuses of 5-day old B6 pups. Data are representative of 3 independent experiments (pooled thymic lobes from n>10 mice per group per experiment). **(h-j)** Flow cytometry profiles of thymic $\gamma\delta^{TN}$, $\gamma\delta^{17}$ and $\gamma\delta^{IFN}$ cells from 7-day FTOC of E15 thymic lobes either with media containing low (5mM) or high (25mM) glucose **(h)**, or with or without 2-deoxy-d-glucose (2-DG) **(i)** or metformin **(j)**. Histograms show the number of $\gamma\delta^{17}$ cells (2-DG $p=0.0013$; metformin $p=0.0426$) and $\gamma\delta^{17}/\gamma\delta^{IFN}$ cell ratio (glucose $p=0.0354$; 2-DG $p<0.0001$; metformin $p=0.0079$). Data are representative of 2 **(h)** or 3 **(i-j)** independent experiments (at least 4 lobes pooled per group per experiment). Error bars show mean ± SEM or SD, *$p < 0.05$, **$p < 0.01$, ***$p < 0.001$, ****$p < 0.0001$ using unpaired or paired two-tailed Student's t-test or One-way ANOVA test with Tukey's multiple comparisons test.

Europe PMC Funders Author Manuscripts

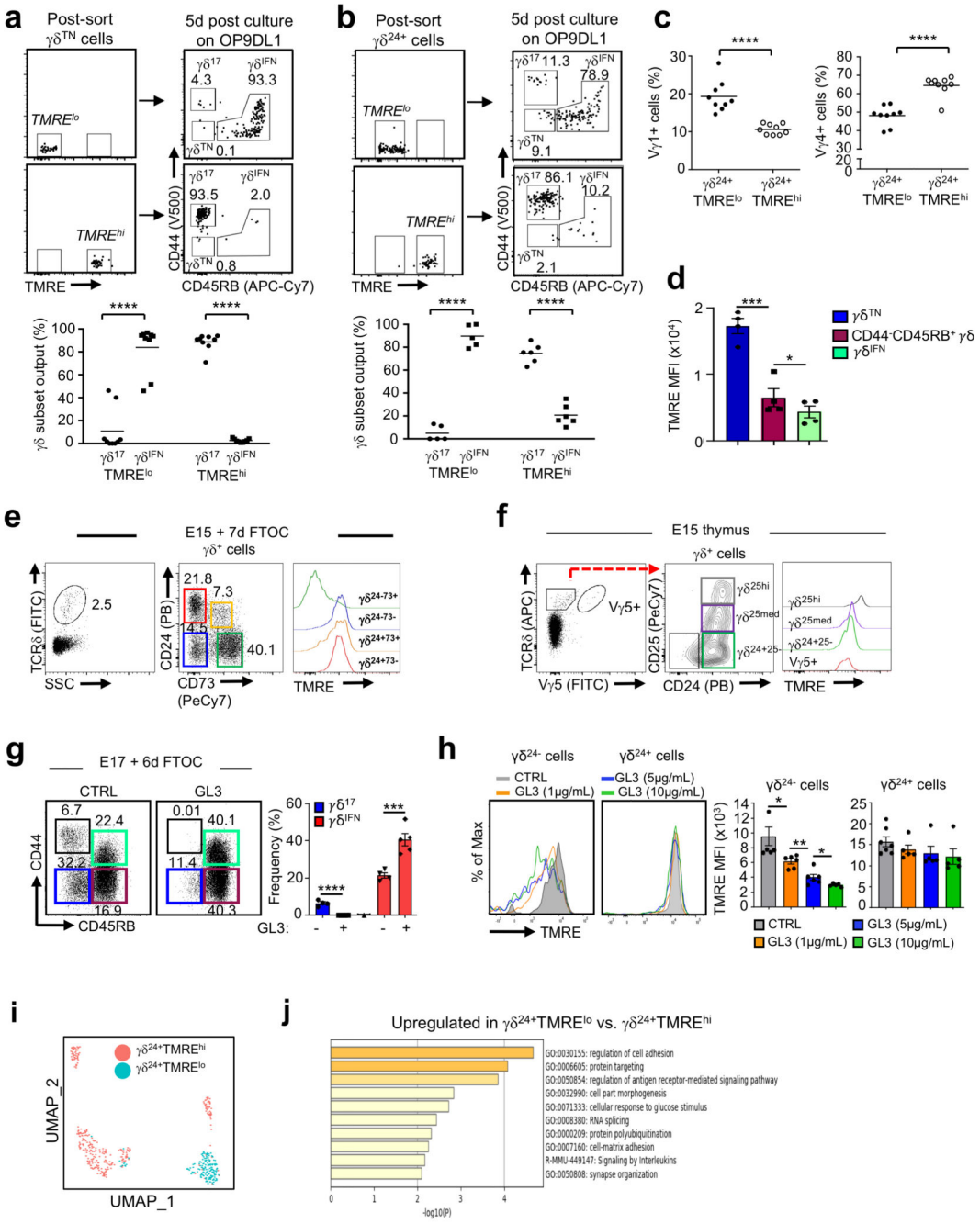

Figure 4. Distinct mitochondrial activities underlie effector fate of thymic γδ T cell progenitors.

(a,b) Flow cytometry profiles and percentage of thymic $\gamma\delta^{17}$ and $\gamma\delta^{IFN}$ cell output from sorted $TMRE^{lo}$ and $TMRE^{hi}$ $\gamma\delta^{TN}$ cells **(a)** or $\gamma\delta^{24+}$ cells **(b)** after 5-day culture on OP9DL1 cells. Data are representative of 3 independent experiments (n = 4 mice pooled per group per experiment). **(c)** Percentage of $V\gamma1^{+}$ and $V\gamma4^{+}$ cells in $TMRE^{lo}$ and $TMRE^{hi}$ $\gamma\delta^{24+}$ progenitors. $V\gamma1^{+}$ $TMRE^{lo}$ vs $TMRE^{hi}$ $p<0.0001$ and $V\gamma4^{+}$ $TMRE^{lo}$ vs $TMRE^{hi}$ $p<0.0001$. Data are representative of 3 independent experiments (cells sorted from n=4 mice pooled per group per experiment). **(d)** TMRE MFI of thymic $\gamma\delta^{TN}$ ($CD44^{-}CD45RB^{-}$),

$CD24^{-}CD44^{-}CD45RB^{+}$ γδ T cells and $γδ^{IFN}$ cells ($CD44^{+}CD45RB^{+}$) from 6-day FTOC of E17 B6 thymic lobes; $γδ^{TN}$ vs $CD44^{-}CD45RB^{+}$ γδ T cells (p=0.002); and $CD44^{-}CD45RB^{+}$ γδ T cells vs $γδ^{IFN}$ cells (p=0.0301). Data are representative of 2 independent experiments (n=4 thymi pooled per point per group and per experiment). **(e)** TMRE staining in $CD24^{-}CD73^{+}$, $CD24^{-}CD73^{-}$, $CD24^{+}CD73^{+}$ and $CD24^{+}CD73^{-}$ γδ T cells from 7-day FTOC of E15 B6 thymic lobes. **(f)** TMRE staining in $CD25^{-}CD24^{+}$ ($γδ^{24+}$ cells), $CD25^{med}$, $CD25^{hi}$ and $Vγ5^{+}$ γδ progenitors from E15 thymus. **(g)** Flow cytometry profiles of thymic $γδ^{TN}$, $γδ^{17}$ and $γδ^{IFN}$ cells from 6-day FTOC of E17 B6 thymic lobes stimulated or not with anti-TCRδ mAb (GL3; 1μg/ml). Graph shows percentage of $γδ^{17}$ (-GL3 vs +GL3; p<0.0001) and $γδ^{IFN}$ (-GL3 vs +GL3; p=0.0002) cells in each condition. Data are representative of 2 independent experiments (n=4 thymi pooled per point per group and per experiment). **(h)** FACS-sorted $γδ^{24+}TMRE^{hi}$ cells from E17 thymi were cultured (or not) for 5h with different concentrations (as indicated) of anti-TCRδ mAb (GL3). TMRE levels were analysed by flow cytometry in $γδ^{24-}$ and $γδ^{24+}$ cells. CTRL vs GL3 (1 μg/mL), p=0.0271; GL3 (1 μg/mL) vs GL3 (5 μg/mL), p=0.0021 and GL3 (5 μg/mL) vs GL3 (10 μg/mL), p=0.0475). Data are representative of 2 independent experiments (n=3 mice pooled per group per experiment). **(i)** Single-cell RNAseq clustering of $TMRE^{lo}$ and $TMRE^{hi}$ $γδ^{24+}$ cells from E15 + 2d FTOC using UMAP. **(j)** GO term analysis of genes upregulated in $TMRE^{lo}$ versus $TMRE^{hi}$ $γδ^{24+}$ cells shown in (i). Error bars show mean ± SD, *p < 0.05, **p < 0.01, ***p < 0.001, ****p < 0.0001 using unpaired two-tailed Student's t-test.

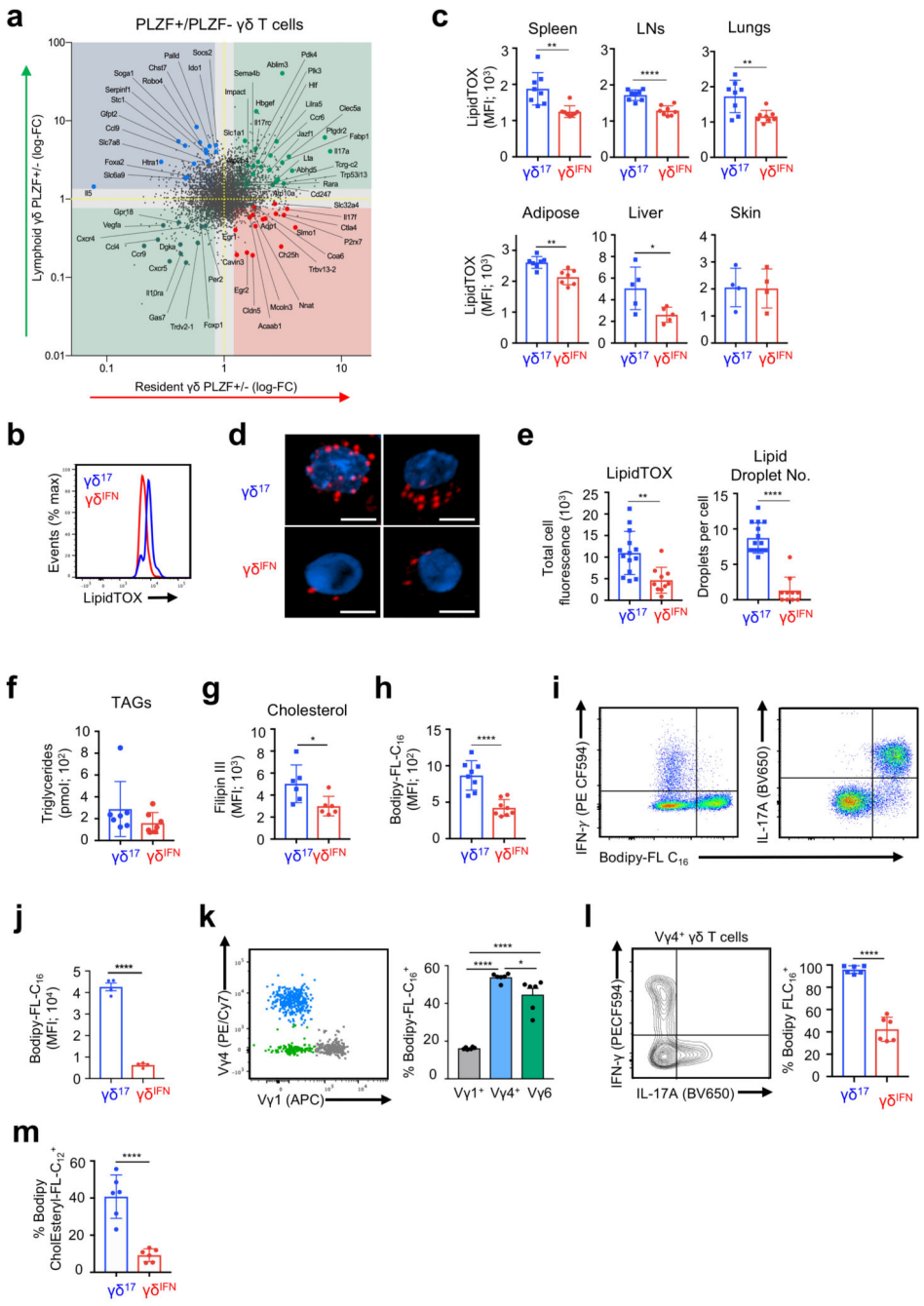

Figure 5. γδ^{17} cells show higher lipid uptake and lipid droplet content than γδ^{IFN} cells.

(a) Quadrant plot of genes upregulated in bulk RNA-sequencing of tissue resident PLZF^{+} γδ T cells (lower right), lymphoid PLZF^{+} γδ T cells (upper left), PLZF^{+} γδ T cells from all tissues (upper right) or PLZF^{-} γδ T cells from all tissues (lower left). Cells were isolated from PLZF-GFP (*Zbtb16*^{GFP}) mice. **(b)** Representative histogram of neutral lipid staining (LipidTOX) in γδ^{17} (CD27^{-}) and γδ^{IFN} (CD27^{+}) cells from LNs *ex vivo*. **(c)** LipidTOX MFI in γδ^{17} and γδ^{IFN} cells from spleen (p=0.0021), LNs (p<0.0001), lungs (p=0.0043), adipose (p=0.0018), liver (p=0.031) and skin (p=0.9442) (n=5-8, data pooled from 2

independent experiments). **(d)** Confocal imaging of $\gamma\delta^{17}$ and $\gamma\delta^{IFN}$ cells expanded *in vitro* and stained with LipidTOX (red) and Hoechst 33342 (blue). Scale bar represents 5μM (data representative of a minimum 10 images from 2 independent experiments). **(e)** Quantification of confocal imaging as shown in (d) (each data point represents the average per cell per image; LipidTOX p=0.0018; lipid droplet no. p<0.0001). **(f)** Quantification of triglyceride (TAG) levels from $\gamma\delta^{17}$ and $\gamma\delta^{IFN}$ cells expanded *in vitro* (n=7, each symbol represents one biological replicate). **(g)** Filipin III staining of $\gamma\delta^{17}$ and $\gamma\delta^{IFN}$ cells *ex vivo* from LNs. Representative histogram (left) and MFI (right) (n=6, data pooled from 2 independent experiments; p=0.0276). **(h)** Representative histogram of Bodipy-FL-C_{16} uptake in $\gamma\delta^{17}$ and $\gamma\delta^{IFN}$ cells from LNs *ex vivo* (n=8, data pooled from 2 independent experiment). **(i)** Representative plots of Bodipy-FL-C_{16} uptake and IL-17 or IFN-γ production by $\gamma\delta^{17}$ and $\gamma\delta^{IFN}$ cells from LNs stimulated with PMA/ionomycin. **(j)** Bodipy-FL-C_{16} MFI in IFN-γ^+ and IL-17^+ γδ T cells (n=4, data representative of 3 independent experiments). **(k)** Representative plot of Vγ1 and Vγ4 expression in total γδ T cells and percentage Bodipy-FL-C_{16} uptake by LN γδ T cell subsets (V$\gamma1^+$, V$\gamma4^+$, V$\gamma1^-4^-$) (n=6, data pooled from 2 independent experiments; Vγ1 vs Vγ4/Vγ6 p<0.0001; Vγ4 vs Vγ6 p=0.0143). **(l)** Representative IFN-γ and IL-17 production by V$\gamma4^+$ γδ T cells from LNs and percentage Bodipy-FL-C_{16} uptake by V$\gamma4^+$IFN-γ^+ and V$\gamma4^+$IL-17^+ γδ cells (n=6, data pooled from 2 independent experiments). **(m)** Percentage Bodipy CholEsteryl FL-C_{12} uptake by $\gamma\delta^{17}$ ($CD27^-$) and $\gamma\delta^{IFN}$ ($CD27^+$) cells from LNs *ex vivo* (n=6, data pooled from 2 independent experiments). Error bars show mean ± SD, *p < 0.05, **p < 0.01, ***p < 0.001, ****p < 0.0001 using unpaired two-tailed Student's t-test.

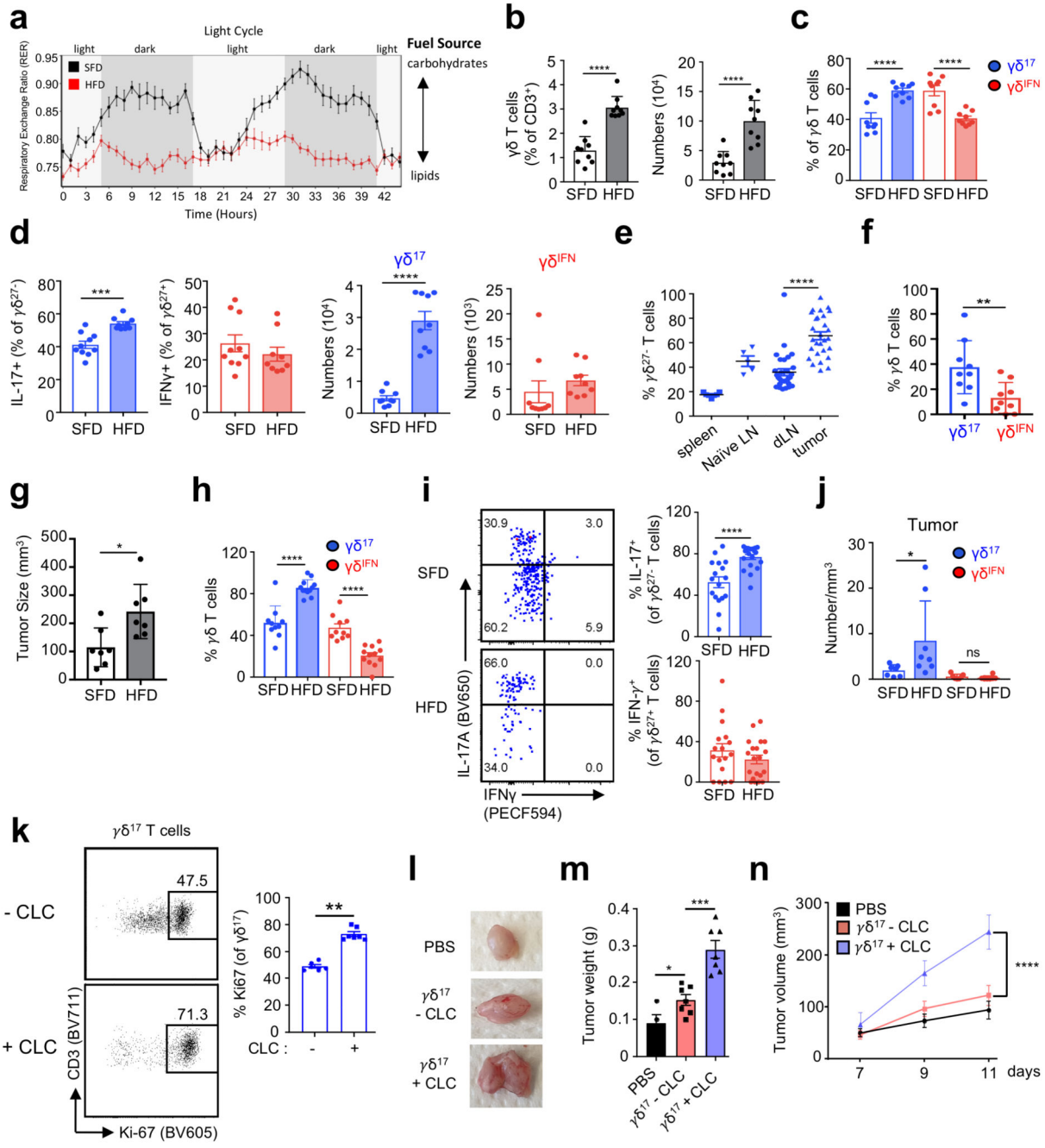

Figure 6. High fat diet promotes the expansion of pro-tumoral γδ^{17} cells in lymph nodes and within tumors.

(a) Respiratory exchange ratio (RER) of mice fed SFD or HFD for 8 weeks (n=3, data from 1 experiment). **(b)** Bar graphs showing the percentage and absolute numbers of CD3$^+$ γδ T cells from LNs of standard fat diet (SFD) and high fat diet (HFD) mice (n=9, data pooled from 3 independent experiments). **(c)** Proportion of γδ^{17} (CD27$^-$) and γδ^{IFN} (CD27$^+$) T cells in LNs of SFD and HFD fed mice (n=9, data pooled from 3 independent experiments). **(d)** Percentage and absolute numbers of CD27$^+$ IFN-γ$^+$ and CD27$^-$ IL-17$^+$ γδ T cells from

LNs of SFD and HFD mice (n=9, data pooled from 3 independent experiments). **(e)** Proportion of infiltrating $\gamma\delta^{17}$ cells in spleen, draining LN and tumor in the B16 tumor model (dLN and tumor n=30, data pooled from 4 independent experiments, spleen n=7, naïve LN n=5). **(f)** Bar graph showing the percentage of $\gamma\delta^{17}$ and $\gamma\delta^{IFN}$ cells infiltrating tumors (n=9, data pooled from 2 experiments). **(g)** Bar graph represents the size of s (mm^3) in SFD and HFD fed mice. (n=7, representative of 3 independent experiments). **(h)** Bar graph showing proportion of infiltrating $\gamma\delta^{17}$ ($CD27^{-}$) and $\gamma\delta^{IFN}$ ($CD27^{+}$) cells in tumors of SFD and HFD fed mice (SFD n=10, HFD n=12, data pooled from 2 independent experiments). **(i)** Representative plots of IL-17 and IFN-γ expression in γδ T cells infiltrating tumors of SFD and HFD fed mice. Bar graphs represent the percentage of $\gamma\delta^{17}$ and $\gamma\delta^{IFN}$ cells infiltrating tumors (SFD n=17, HFD n=20, data pooled from 3 independent experiments). **(j)** Bar graph showing the number/mm^3 of $\gamma\delta^{17}$ and $\gamma\delta^{IFN}$ cells in tumors of mice on SFD or HFD (SFD n=7, HFD n=8, data pooled from 2 independent experiments). **(k)** Plots of proliferating $Ki67^{+}$ $\gamma\delta^{17}$ cells cultured for 5h with or without cholesterol-loaded cyclodextrin (CLC). Graph represents the percentage of $Ki67^{+}$ $\gamma\delta^{17}$ cells (data are representative of two independent experiments; pool of 3-5 mice per experiment). **(l)** $\gamma\delta^{17}$ cells cultured (or not) with cholesterol-loaded cyclodextrin (CLC) for 5h were injected s.c. into E0771 tumors at d7 and d9 after tumor cell injection. Representative picture of tumors observed at day 11 post-E0771 cell inoculation. **(m)** Graph showing tumor weight at day 11 post-E0771 inoculation. CTRL vs $\gamma\delta^{17}$-CLC ($p=0.0361$); $\gamma\delta^{17}$-CLC vs $\gamma\delta^{17}$+CLC ($p=0.0003$). **(n)** E0771 tumor growth was monitored every two days after inoculation. (l-n) data are representative of three independent experiments (n=3 mice per experiment); $p<0.0001$. Error bars show mean ± SD, *$p < 0.05$, **$p < 0.01$, ***$p < 0.001$, ****$p < 0.0001$ using unpaired two-tailed Student's t-test or one-way ANOVA test with Sidak post-hoc analysis.

Europe PMC Funders Author Manuscripts

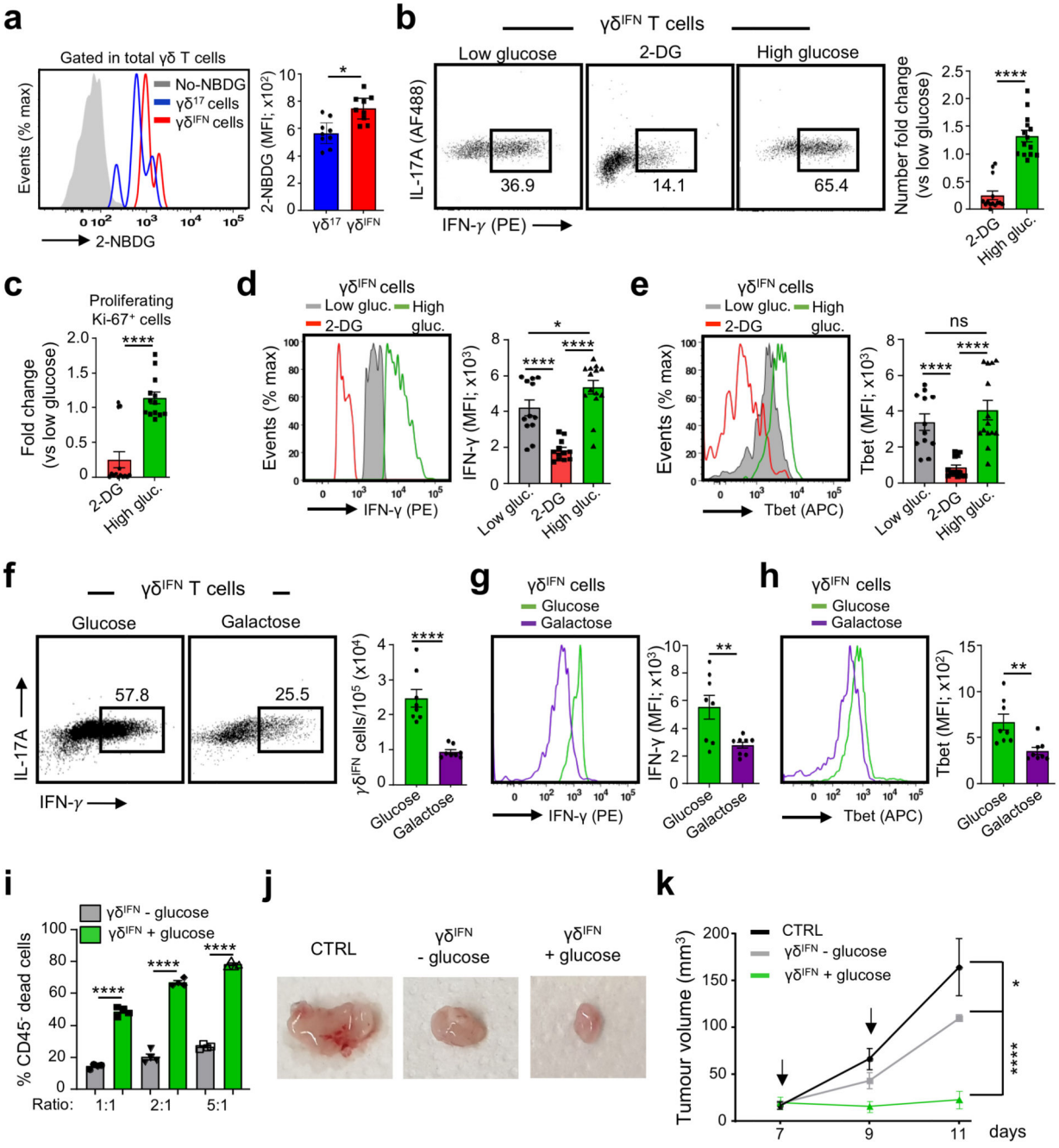

Figure 7. Glucose supplementation enhances the anti-tumor effector functions of γδ^{IFN} cells.

(a) Glucose uptake assessed upon i.v. injection of fluorescent 2-NBDG in tumor-bearing mice. Tumors were harvested 15 min later for analysis. Histogram represents 2-NBDG uptake in γδ^{17} and γδ^{IFN} cells (p=0.047). Data are representative of 2 independent experiments (n = 4 mice per group and per experiment). **(b-i)** Purified splenic and peripheral lymph nodes γδ^{IFN} T cells (CD3^{+}TCRγδ^{+}CD27^{+}) were cultured in the presence of IL-7 with media containing low glucose (5mM), 2-deoxyglycose (2-DG), high glucose (50mM) or galactose (20mM) for 78h. **(b)** Plots of peripheral γδ^{IFN} T cells cultured with IL-7 and

media containing low glucose, 2-DG or high glucose. Histogram represents the fold change in number of $\gamma\delta^{IFN}$ T cells cultured with 2-DG or high glucose versus low glucose ($p<0.0001$). **(c)** Fold change in number of proliferating Ki-67^{+} $\gamma\delta^{IFN}$ cells cultured with 2-DG or high glucose versus low glucose ($p<0.0001$). **(d)** IFN-γ expression was analysed by flow cytometry in $\gamma\delta^{IFN}$ cells incubated with media containing low glucose, 2-DG or high glucose. Histograms show the MFI of IFN-γ. Low glucose vs 2-DG ($p<0.0001$); 2-DG vs High glucose ($p<0.0001$); Low glucose vs high glucose ($p=0.0115$). **(e)** Tbet expression was analysed by flow cytometry in $\gamma\delta^{IFN}$ cells incubated with media containing low glucose, 2-DG or high glucose. Histograms show the MFI of Tbet. Low glucose vs 2-DG ($p<0.0001$); 2-DG vs High glucose ($p<0.0001$). **(f)** Flow cytometry profiles of peripheral $\gamma\delta^{IFN}$ T cells cultured with IL-7 and media containing glucose (50mM) or galactose (20mM). Histogram represents the numbers of $\gamma\delta^{IFN}$ T cells ($p<0.0001$). **(g,h)** IFN-γ **(g)** and T-bet **(h)** expression was analysed by flow cytometry in $\gamma\delta^{IFN}$ cells incubated with media containing glucose or galactose ($p=0.0085$ for IFN-γ expression and $p=0.0034$ for Tbet expression). Histograms show the MFI of IFN-γ and T-bet. **(i)** Summary of killing assay *in vitro* of E0771 tumor cells by $\gamma\delta^{IFN}$ T cells previously supplemented (or not) with glucose (5h pre-incubation); $p<0.0001$. Data are representative of 2 independent experiments (n = 3 mice per group and per experiment). **(j)** Representative picture of tumors observed at day 11 post-E0771 inoculation. $\gamma\delta^{IFN}$ cells supplemented (or not) with glucose for 5h were injected into the tumor at d7 and d9 after tumor cell injection. **(k)** The E0771 tumor growth was monitored every two days during 11 days after E0771 inoculation. CTRL vs $\gamma\delta^{IFN}$ - glucose ($p=0.0148$); $\gamma\delta^{IFN}$-glucose vs $\gamma\delta^{IFN}$+ glucose ($p<0.0001$). (b-e) Data are representative of 4 independent experiments (n = 3 mice per group and per experiment); (f-h) Data are representative of 2 independent experiments (n = 4 mice per group and per experiment), (j,k) Data are representative of 2 independent experiments (n = 5 mice per group and per experiment). Error bars show mean ± SEM, *$p < 0.05$, **$p < 0.01$, ***$p < 0.001$, ****$p < 0.0001$ using unpaired two-tailed Student's t-test or ANOVA test.